RESEARCH ARTICLE

Synoptic-scale and mesoscale controls for tornadogenesis on cold fronts: Shear-zone vortex-genesis in a developing frontal wave

M. R. Clark[1,2,3] | **D. J. Parker[2,4]** | **K. E. Hanley[5]**

[1]Met Office, Exeter, UK

[2]University of Leeds, Leeds, UK

[3]Tornado and Storm Research Organisation (TORRO), Oxford, UK

[4]NORCE Norwegian Research Center, Bjerknes Center for Climate Research, Bergen, Norway

[5]MetOffice@Reading, University of Reading, Reading, UK

Correspondence
M. R. Clark, Met Office, FitzRoy Road, Exeter, EX1 3PB, UK.
Email: matthew.clark@metoffice.gov.uk

Abstract

High-resolution model simulations and radar observations are used to investigate the onset of vortex-genesis in a tornadic narrow cold-frontal rain band (NCFR). The timing and location of vortex-genesis was strongly constrained by a developing frontal wave, which tracked northeast across the United Kingdom and Ireland on 17 October 2011. In the simulations, vortices occurred preferentially during the early stages of wave development and just down-front of the wave centre, where large increases in vertical vorticity occurred in concert with decreases in the cross-frontal confluence. Vortex-genesis ceased as the frontal wave matured, due to the onset of frontal fracture. Two distinct scales of vortex-genesis are documented: primary vortex-genesis on the meso-γ-scale, and secondary vortex-genesis on the miso-scale. We show that horizontal shearing instability is the most likely vortex-genesis mechanism, consistent with previous theoretical work on the stability of vertical vortex strips in the presence of horizontal stretching deformation. Secondary vortices occurred along the braid regions between primary vortices where the shear zone became particularly narrow and intense. In the model, these vortices developed extremely rapidly (from small perturbations to maximum vertical vorticity in 5–15 min) and the strongest exhibited near-surface vertical vorticity maxima approaching 10^{-1} s^{-1}. Vortices of both scales were associated with characteristic local perturbations in the NCFR and we show, by comparison with radar reflectivity data, that primary and secondary vortices were likely present in the real NCFR. Tornado reports were associated with small NCFR perturbations like those associated with the secondary vortices in the model simulations. Analysis of the sub-structure of individual simulated vortices suggests that tornado-genesis is most likely within a region of intense near-surface vertical vorticity stretching at the north or northwest flank of the secondary vortices.

KEYWORDS

cold front, horizontal shearing instability, narrow cold-frontal rainband, tornado, vortex strip, vortex-genesis

1 | INTRODUCTION

Recent climatologies suggest that the United Kingdom experiences an average of approximately 30 tornadoes per annum (Reynolds, 1999; Kirk, 2007; Mulder and Schultz, 2015), of which 40–50% are associated with precipitation systems exhibiting quasi-linear morphologies in radar rainfall imagery (Mulder and Schultz, 2015; Clark and Smart, 2016). An important type of quasi-linear precipitation system is the narrow cold-frontal rainband (NCFR: Houze *et al.*, 1976). These systems, which are responsible for approximately one-third of the United Kingdom's tornadoes, are characterised by strong but relatively shallow updraughts forced by horizontal convergence at the frontal boundary. In NCFR-bearing fronts the near-surface frontal boundary is marked by a narrow zone of strong cyclonic relative vertical vorticity (i.e. a vertical vortex sheet, or "vortex strip") and large horizontal temperature gradient. Observational and modelling studies have shown that NCFR tornadoes are associated with meso-γ- to miso-scale vortices that develop along this vortex sheet.[1] Vortex-genesis has generally been attributed to horizontal shearing instability (HSI) (e.g. Matejka *et al.*, 1980; Carbone, 1982; 1983; Hobbs and Persson, 1982; Lee and Wilhelmson, 1997; Smart and Browning, 2009), though the mechanism of formation is not universally agreed upon and it may differ from case to case.

Clark and Parker (2020) (hereafter CP20) analysed a set of 114 NCFRs (44 tornadic) to identify synoptic situations favouring tornadoes and to find environmental parameters capable of distinguishing between tornadic and non-tornadic cases. At least 55% of tornadic NCFRs were found to be associated with secondary cyclogenesis (i.e. a developing frontal wave) along a trailing frontal system. Events producing ≥7 tornadoes showed an even stronger association with frontal waves (72% of cases). Wave development resulted in large spatio-temporal changes in the magnitude of environmental parameters found to have skill in discriminating between tornadic and non-tornadic events. In particular, a bulk measure of the cross-frontal shear vorticity (hereafter shear vorticity) increased rapidly near the wave centre, whilst the speed of the front-normal flow component on the cold side of the front (hereafter $-v'_{cold}$) increased steadily down-front of the wave centre (i.e. in the along-front direction pointing towards higher

geopotential height), where the front bulged forward on the meso-α-scale.

A generalised measure of tornado probability, p[TN], based on a combination of shear vorticity and $-v'_{cold}$ (see figure 3 of CP20) was found to reach a maximum immediately down-front of the wave centre, increasing rapidly during the early stages of wave development. CP20 suggested that increases in the shear vorticity, especially when coupled with decreases in the horizontal strain (i.e. stretching deformation), favoured the onset of vortex-genesis due to horizontal shearing instability (HSI) in this region, a hypothesis consistent with previous theoretical and modelling work on the stability of two-dimensional vortex strips in variable strain fields (Dritschel *et al.*, 1991; Bishop and Thorpe, 1994). Tornadogenesis is assumed to occur in association with some of the resulting small-scale vortices, consistent with previous modelling and radar studies of tornadic NCFRs. If correct, the scenario described constitutes an important link between the synoptic scale and the meso-γ- to miso-scales in frontal waves. The purpose of this article is to demonstrate in one case-study, using observations and high-resolution model simulations, how a frontal wave constrains the timing and location of meso-γ- to miso-scale vortex-genesis, and therefore the area at risk of tornadoes, supporting the hypothesis of CP20 for tornadic NCFRs in frontal waves. The event under study, which occurred on 17 October 2011, produced at least two tornadoes over the United Kingdom (Brown and Meaden, 2012). Although the models used in this study are not capable of resolving a circulation on the scale of a typical NCFR tornado,[2] we show that they produce numerous meso-γ- to miso-scale shear-zone vortices (i.e. with diameters in the typical range 1–10 km) in the area where tornadoes were reported in the real NCFR.

The remainder of the article is structured as follows. The model set-up is described in Section 2 and key parameters are defined. An overview of the synoptic-scale situation is given in Section 3, and the main features of frontal wave development are described using observations and output from a 1.5 km grid-length model. Primary shear-zone vortex-genesis and its relationship to the developing frontal wave is described in Section 4, and the life cycle of an individual primary vortex is described in Section 5. A more detailed exploration of primary and secondary shear-zone vortex-genesis, and of the three-dimensional structure of secondary vortices,

---

[1]In this study we use the mesoscale subdivisions of Orlanski (1975): meso-α-scale: 200–2,000 km; meso-β-scale: 20–200 km; meso-γ-scale: 2–20 km. However, in the case of vortices of diameter ≤∼4 km, we use the prefix "miso-", to ensure consistency with existing nomenclature (i.e. "misocyclones": Fujita, 1981).

[2]A 100 m grid-length configuration of the same model was, however, shown to be capable of resolving the circulation associated with a large (∼1 km diameter) tornado in a supercell thunderstorm (Hanley *et al.*, 2016), demonstrating that it is capable of resolving features on a similar scale to cold-frontal misocyclones.

is presented in Section 6 using output from a 300 m grid-length model, and associated perturbations in the modelled NCFR are compared with radar observations of the real NCFR near to the reported tornadoes. Discussion follows in Section 7 and a synthesis of the results is presented in Section 8, in the form of a conceptual model. Finally, a summary of the key findings is given in Section 9.

2 | DATA AND METHODS

2.1 | Model description

Data from two convection-permitting configurations of the Met Office's Unified Model (Davies *et al.*, 2005; Wood *et al.*, 2014) are presented in this study. Both were run using the Regional Atmosphere and Land 2.0 midlatitude configuration (RAL2-M). The first is the 1.5 km grid-length version, which is run for a domain spanning approximately 44–64°N and 26°W–17°E. We use this model to explore the development of the frontal wave, its influence on the spatio-temporal evolution of shear vorticity, $-v'_{\text{cold}}$ and confluence at the cold front, and the wave-relative location and timing of meso-γ-scale vortex-genesis. The model uses a semi-implicit, semi-Lagrangian numerical scheme with a 1-min time step and runs on a rotated latitude–longitude horizontal grid with Arakawa C staggering. In the vertical the grid is stretched and, close to the surface, terrain-following, transitioning to horizontal at the model top ($z = 40$ km), with Charney–Phillips staggering and 70 vertical levels. The vertical grid length is smallest close to the surface and the vertical stretching is quadratic over much of the vertical extent of the domain. The first model level above the surface is at $z = 2.5$ m for the horizontal wind components and air density, and $z = 5$ m for other parameters. The model uses a Smagorinsky-type turbulence closure scheme. The lower boundary conditions, as described in Wood *et al.* (2014), impose surface stresses that can contribute to vorticity generation. The terrain is defined using a smoothed version of the 100 m resolution Shuttle Radar Topography Mission (SRTM) data. The 1.5 km model takes its boundary conditions from the global Unified Model, which for the purposes of this study was rerun using an initialisation time of 0000 UTC 16 October 2011, taking data from the Met Office global operational analysis. The global model was run at n768 resolution using the Global Atmosphere 6.1 configuration (Walters *et al.*, 2017). Output is analysed for the period 0800 UTC 17 October to 0000 UTC 18 October (i.e. t + 32 hr to t + 48 hr, where t + 0 hr is the model initialisation time).

The second model has a horizontal grid-length of 300 m and a time step of 12 s over a domain of 600 × 600 km centred on the Irish Sea. As with all configurations of the Unified Model, this uses semi-implicit, semi-Lagrangian discretisation of the deep atmosphere, non-hydrostatic Euler equations, which allows stable integrations with long time steps. This fine-scale model was also initialised from the 0000 UTC 16 October 2011 Met Office global analysis, but it takes its lateral boundary conditions from the 1.5 km model. Vertical levels are as for the 1.5 km model and the terrain is again defined using smoothed 100 m resolution SRTM data. We use this model to further explore the structure, development and evolution of primary (meso-γ-scale) and secondary (miso-scale) vortices, and for comparison of the associated structures in the rainfall field with radar observations of the real NCFR, especially near to the reported location of tornadoes.

2.2 | Definition of bulk parameters

Bulk environmental parameter values are calculated from ERA-Interim (hereafter ERAi) data (Dee *et al.*, 2011) and the 1.5 km model output fields using the methodology of CP20 (a full description can be found in their Sections 2.2 and 2.3). A natural coordinate system is adopted in which x' is tangential to the local front and points towards lower geopotential height, and in which y' is normal to the local front and points towards the cold air. The term up-front will be taken as the positive x' direction, that is, pointing along the local front in the direction of lower geopotential height; an observer looking up-front would have the cold air on their left. The term down-front will be taken as the negative x' direction, that is, pointing along the front in the direction of higher geopotential height (for a graphical depiction of the coordinate system, see inset panel in Figure 1b). Analysis points are defined at regular intervals along the surface frontal boundary ("on-front analysis points"). For the analysis using ERAi data, frontal positions are taken from Met Office surface analysis charts. For the analysis using 1.5 km model data, the frontal boundary is taken to be the location of maximum near-surface vertical vorticity and collocated horizontal temperature gradient in the model fields. For convenience, analysis points are defined wherever the frontal boundary (as defined above) crosses a whole degree of latitude or longitude, though spacing is reduced to 0.5° latitude or longitude where the front exhibits substantial curvature, in order to adequately capture the shape of the front. At each point, finite differences are calculated between values at corresponding warm-air and cold-air analysis points located 150 km from the front in the local front-normal direction. To reduce the impact of small-scale variability in the 1.5 km model fields, the parameter value at each point is taken to be the mean value over nine grid squares centred
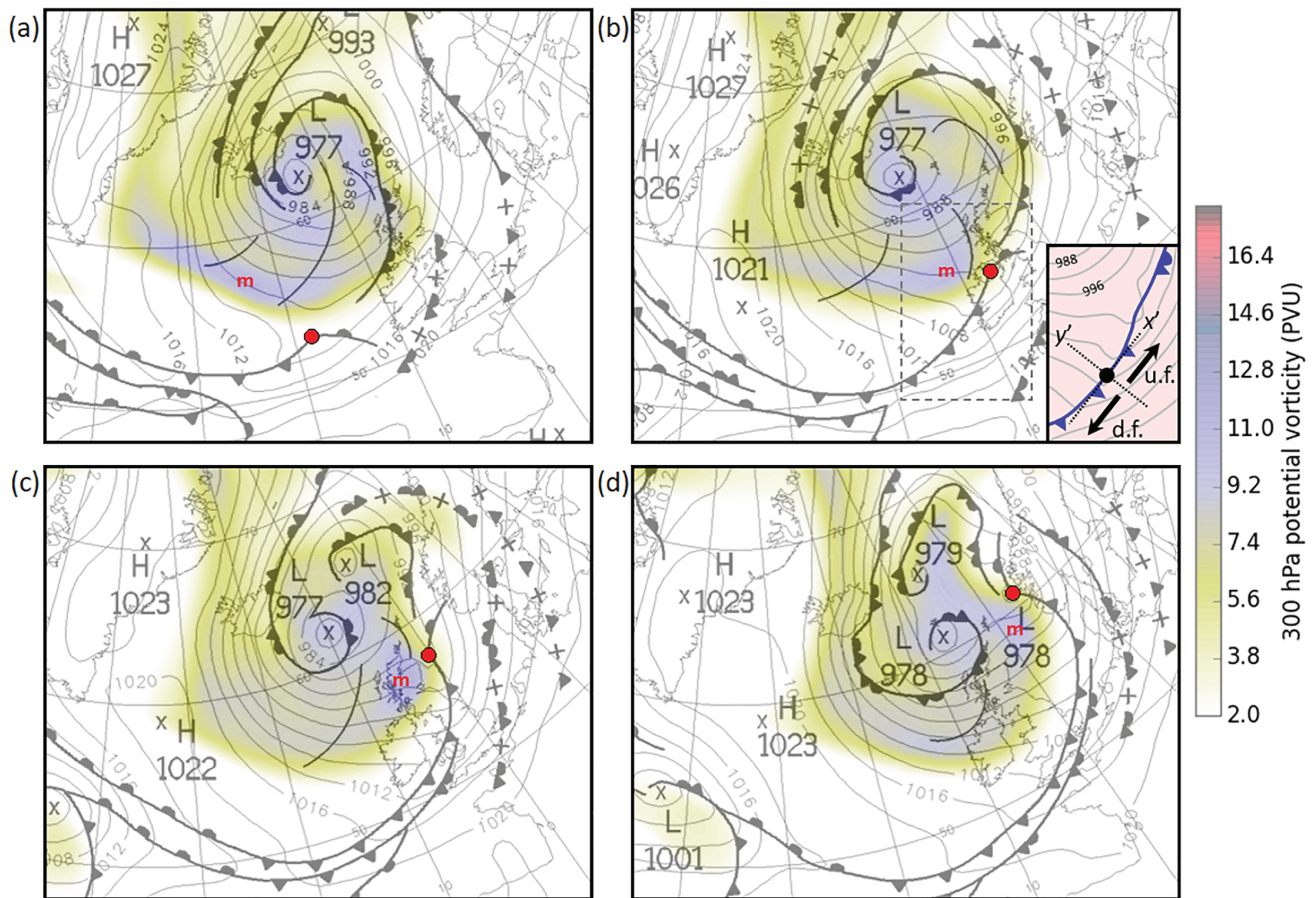
FIGURE 1 Sequence of Met Office surface analysis charts showing evolution of the frontal wave (the centre of which is marked by a red dot) on 17–18 October 2011. Shading shows ERAi 300 hPa potential vorticity (PV). "m" denotes the approximate centre of the local PV maximum associated with frontal wave development. (a) 0600 UTC 17th; (b) 1200 UTC 17th; (c) 1800 UTC 17th; (d) 0000 UTC 18th. The inset in (b) shows axes of the natural coordinate system (dashed lines) at the point marked by the black dot, in which x' is tangential to the local front and y' is normal to the local front and points towards the cold air. Bold arrows and annotations "u.f." and "d.f." denote the up-front and down-front directions, respectively. Grey lines are isobars at 4 hPa intervals. For context, the domain of the inset panel is indicated by the dashed grey box in the main panel [Colour figure can be viewed at wileyonlinelibrary.com]

on the analysis point (i.e. a square of 4.5×4.5 km). Whilst 150 km is rather far from the front, sensitivity studies conducted using a range of separation distances between 25 and 600 km (not shown) revealed that the u' and v' winds are relatively insensitive to the choice of separation distance (i.e. the wind field is relatively uniform within the pre- and post-frontal air masses). The use of 150 km ensures consistency with CP20, where values were derived using ERAi data only.

A bulk measure of the cross-frontal vorticity (hereafter "shear vorticity") is defined as the difference in the along-front wind component, u', between the warm- and cold-air analysis points, divided by the distance between these points (positive where $u'_{warm} > u'_{cold}$, where positive u' points up-front). A bulk measure of the cross-frontal confluence (hereafter "bulk confluence") is defined in a similar manner by analysis of the difference in the cross-front wind component, v' (positive where

$v'_{warm} > v'_{cold}$ and where positive v' points towards the cold air). The parameter $-v'_{cold}$ is evaluated at the cold-air point. The probability of tornadoes, $p[TN]$, as defined by CP20, depends on the combined values of shear vorticity and $-v'_{cold}$, and describes the conditional risk of one or more tornadoes, derived from analysis of bulk measures for a large set of tornadic and non-tornadic NCFRs (see figure 3 of CP20; empirical formulae for the calculation of $p[TN]$, given shear vorticity and $-v'_{cold}$, are given in Appendix A). The parameter is used here to highlight the region at risk of tornadoes and to show how the evolution of $p[TN]$ relates to the development of the frontal wave.

The advantage of the bulk measures is that they are insensitive to the substantial small-scale variability in parameter values often observed along the shear zone, which tend to mask differences associated with the evolving synoptic- to meso-α-scale environment of the front, which are of interest to this study. Bulk parameters

are calculated at the 1,390 m above ground level (AGL) model level, selected because it is closest to the observed mean 850 hPa geopotential height over the United Kingdom in the current event, therefore ensuring consistency with values derived from ERAi fields here and in CP20. Furthermore, the 1,390 m level is above the friction layer, but below the height of the top of the frontal updraught and shear zone over most of the domain, so that the bulk measures properly represent the horizontal wind differences across the vertical vorticity sheet at the front, without being unduly affected by the variable effects of friction over land and sea areas (which partially mask the along-front variability associated with the frontal wave at lower heights).

Dritschel *et al.* (1991) showed that the barotropic growth of vortices along a vertical vorticity strip (i.e. the release of HSI) is supressed when the stretching deformation acting on the strip exceeds one quarter of the magnitude of the vorticity within the strip. In the natural coordinate system defined above, and assuming the axis of dilatation is aligned with the front, the stretching deformation, D_s, is given by

$$D_s = \frac{\partial u'}{\partial x'} - \frac{\partial v'}{dy'}. \quad (1)$$

The first term represents dilatation in the along-front direction and the second term represents confluence in the cross-front direction. The shear zone at the front in the present case differs from the set-up in Dritschel *et al.* (1991) in that it is characterised by large horizontal convergence in addition to large vertical vorticity (i.e. v' varies substantially across the narrow shear zone itself); in Dritschel *et al.* (1991), v' gradients are associated only with the larger-scale stretching deformation field. In the current case, the bulk measure of confluence, as described above, will include contributions from both the v' difference across the shear zone and the v' difference associated with the larger-scale stretching deformation field, where present. Inspection of the model fields shows the v' difference across the shear zone to be the larger of these two contributions, overall. For this reason, in the local environment of the front, the cross-frontal confluence is much larger than the along-front dilatation.[3] Physically, one would expect cross-frontal confluence to reduce the amplitude of perturbations, by flattening them in the

cross-front direction, regardless of whether this confluence is a feature of the larger-scale environment (as with a stretching deformation field in which the axis of contraction is normal to the front) or localised to the strip, so we consider the results of Dritschel *et al.* (1991) relevant in spite of this difference. An approximate measure of the potential for the release of HSI along the strip may therefore be obtained using the bulk measures of shear vorticity and cross-frontal confluence, under the assumption that the local along-front dilatation is relatively small. The criterion, S_{HSI}, for barotropic vortex-genesis at the shear zone is thus approximated as:

$$S_{HSI} = (4 \times \text{bulk confluence}) - \text{shear vorticity.} \quad (2)$$

Negative values of S_{HSI} indicate an environment favourable for the growth of vortices by the release of HSI, whilst positive values indicate an environment in which the growth of vortices is likely to be supressed by the cross-frontal confluence. Ostensibly, the method assumes that the axis of dilatation of the larger-scale stretching deformation field, where present, is aligned with the front (i.e. the axis of contraction is normal to the front). However, in practice, for constant stretching deformation, the bulk confluence will decrease as the angle between the front and the axis of dilatation increases from 0 to 90°. Therefore, the bulk confluence is sensitive both to changes in the magnitude of stretching deformation and changes in the angle of the axis of dilatation relative to the front.

3 | OVERVIEW OF WAVE DEVELOPMENT AND REPORTED TORNADOES

In this section we provide an outline of frontal wave development on the synoptic- and meso-α-scales, describe the location of tornado reports relative to the wave, and compare the observed wave development with that in the 1.5 km model.

3.1 | Synoptic overview

At 0600 UTC 17 October 2011, a primary cyclone of central pressure 977 hPa was located between Scotland and Iceland (Figure 1a).[4] The cyclone's trailing frontal system intersected northwestern parts of the United Kingdom and Ireland where it was slow moving. An incipient

---

[3]This is shown by calculation of the bulk measures of cross-frontal confluence and along-frontal dilatation using a range of separation distances from 600 to 25 km. As the separation distance decreases, the bulk along-frontal dilatation becomes smaller relative to the bulk cross-frontal confluence. Near the lower limit of the tested range of distances, bulk confluence was ~15 times larger than the bulk along-front dilatation.

[4]Met Office surface analysis charts are created manually by operational meteorologists, using model output and satellite and surface observations (e.g. see Mulqueen and Schultz, 2015).
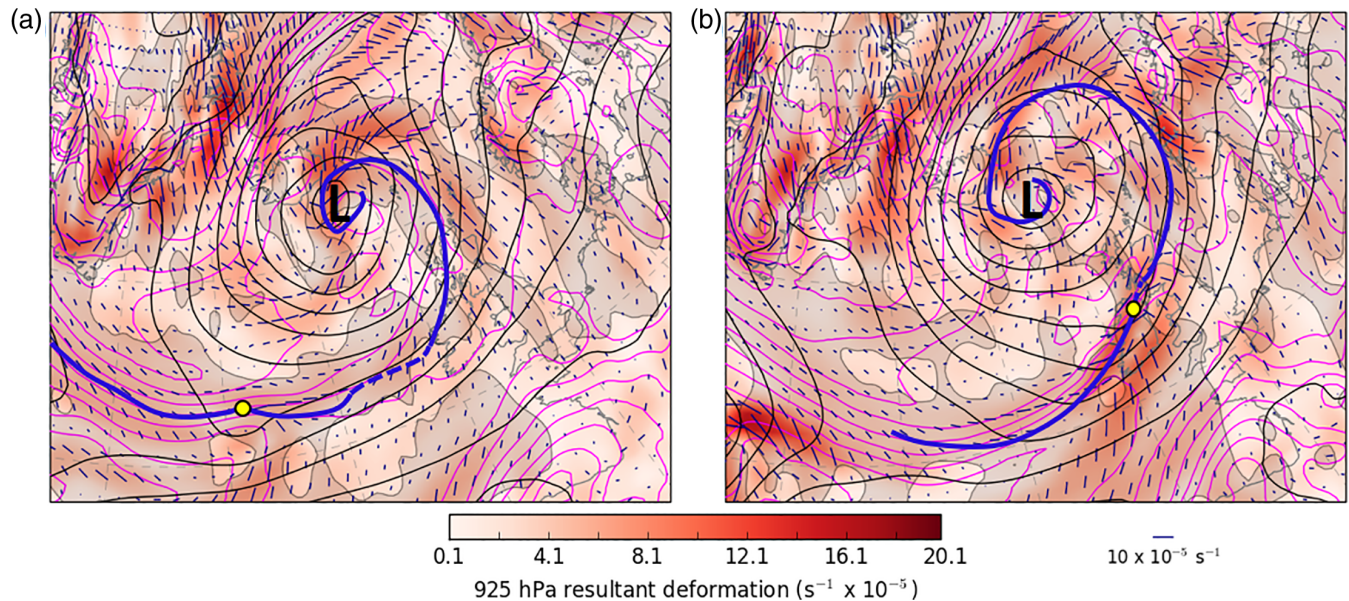
FIGURE 2 Resultant deformation of the horizontal wind field (colour shading) and axis of dilatation (dashes orientated parallel to the axis of dilatation, with dash length proportional to the magnitude of resultant deformation) at (a) 0000 UTC 17 October 2011 and (b) 1200 UTC 17 October 2011, analysed at 925 hPa using ERAi data. Magenta contours denote 925 hPa θ (contour interval 2 K) and black contours 925 hPa geopotential height (contour interval 4 DAM). Grey shading denotes areas where the isotherms are orientated at an angle of <40° to the local axis of dilatation. Bold, blue line indicates location of fronts as shown in Met Office surface analysis charts (only the trailing frontal system of interest is shown; dashed lines indicate sections of front not marked in the corresponding analysis charts (e.g. cf. Figure 1b), but included here for continuity of the trailing frontal system as suggested by the 925 hPa θ field). Yellow circle indicates the centre of the frontal wave and "L" denotes the centre of the parent low-pressure system [Colour figure can be viewed at wileyonlinelibrary.com]

frontal wave is evident further down-front, to the southwest of Ireland. The environment of the trailing front was characterised, for a period of at least 12 hr prior to wave development and continuing through the early phases of development, by substantial resultant deformation, with the axis of dilatation orientated at a small angle to the front (Figure 2). Over the following 12–18 hr, the frontal wave moved northeast and deepened rapidly, crossing Ireland and northern parts of the United Kingdom between 1000 and 1900 UTC (Figure 1b,c). By 0000 UTC 18 October, the wave had matured into a discrete secondary cyclone of central pressure 978 hPa, centred just east of the Norwegian coastline (Figure 1d). Wave development was apparently induced by the approach of an upper-level potential vorticity (PV) maximum towards the front between 0600 and 1200 UTC (shading in Figure 1). After rounding the axis of an upper-level trough, the PV maximum moved northeast in tandem with the deepening surface frontal wave between 1800 UTC 17 and 0000 UTC 18 October (Figure 1c,d).

Bulk measures of relevant environmental parameters, as derived from 850 hPa ERAi fields, exhibit spatio-temporal evolution that closely follows the conceptual model described by CP20 for tornadic frontal waves

(Figure 3; cf. figures 11 and 12 of CP20). Characteristic features include:

- Rapid increases in shear vorticity near the wave centre during the early stages of development (Figure 3a).
- Steady increases in $-v'_{cold}$ (Figure 3b) down-front of the wave centre over a swath several hundred kilometres wide, with an associated, amplifying, meso-α-scale frontal bulge (wavelength of order hundreds of km); for example, as over the North Sea in Figure 3b. This bulge occurs due to the strong positive correlation between $-v'_{cold}$ and the forward speed of the front in the direction normal to its length (hereafter front-normal forward motion [FNFM]: CP20).
- Rapid increases in $p[TN]$ along a relatively narrow swath centred just down-front of the wave apex (i.e. between the developing shear vorticity and $-v'_{cold}$ maxima, and on the up-front flank of the meso-α-scale frontal bulge; Figure 3c).
- Large and increasing frontogenesis near the wave centre during the early stages of development (e.g. over and to the west of Ireland in Figure 3d), followed by decreasing frontogenesis and eventual transition to frontolysis near
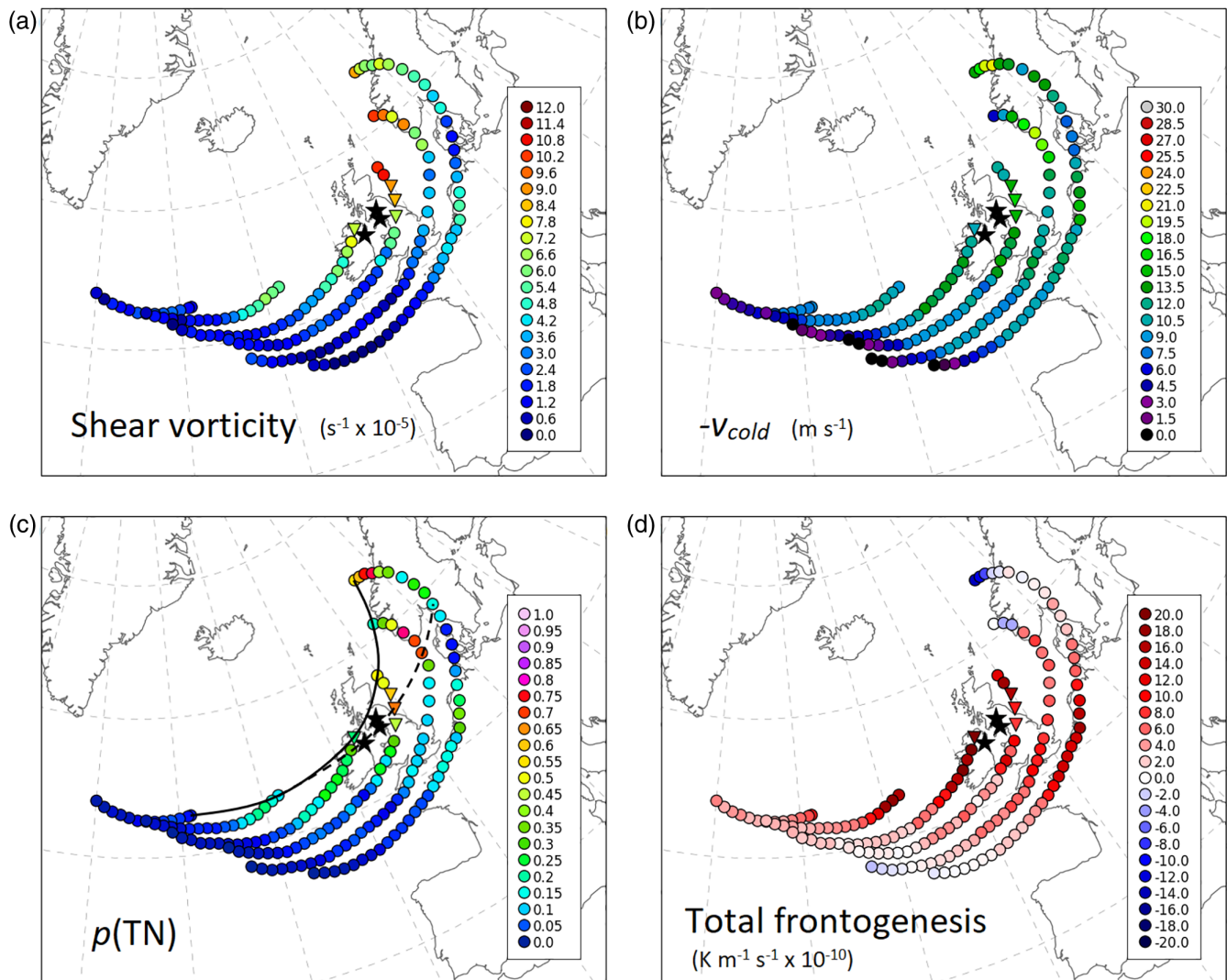
FIGURE 3   Evolution of 850 hPa bulk parameter values, calculated from ERAi reanalysis data, at on-front analysis points at 6 hr intervals between 0000 UTC 17 October and 0600 UTC 18 October 2011, following the methodology of CP20. Frontal positions are taken from the corresponding Met Office surface analysis charts at each analysis time. (a) Shear vorticity; (b) $-v'_{cold}$; (c) $p[TN]$; (d) total frontogenesis (horizontal, kinematic terms only). On-front analysis points are shown by the coloured dots (inverted triangles for points near to tornado reports), with the colour shading indicating the magnitude of the corresponding parameter (see scale within each panel). Star symbols mark the locations of reported tornadoes. In (c), solid black line denotes the track of the centre of the frontal wave, and dashed black line denotes the track of a pseudo-Lagrangian analysis point situated along the tornadic part of the front [Colour figure can be viewed at wileyonlinelibrary.com]

the wave centre by the mature and dissipating stages of development (e.g. over Norway in Figure 3d).

3.2 | Tornadoes of 17 October 2011

At least two tornadoes occurred in association with the frontal wave of 17 October 2011: at Templand, Dumfries and Galloway, just after 1500 UTC and at Whitehaven, Cumbria, at approximately 1540 UTC. A further possible tornado occurred at Killowen, Northern Ireland, at approximately 1300 UTC. Although video footage of the Killowen

event showed an intense vortex making landfall from Carlingford Lough, it was classified by TORRO as an eddy whirlwind (Brown and Meaden, 2012), owing to the frequent occurrence at this location of vortices generated by the interaction of strong winds with the mountains surrounding the lough (the so-called "Carlingford Kettle"), particularly in southerly flow as observed ahead of the cold front in the current case. For the purposes of this study, we choose to include this event as a possible tornado because the reported time closely matches that of NCFR passage at Killowen. However, confidence in the diagnosis of a tornado is lower in this case than for the other two reported
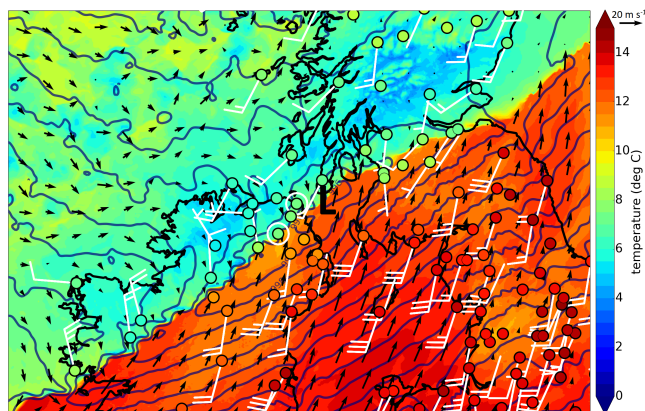
FIGURE 4 Surface wind vectors (black arrows), MSLP (navy-blue contours at 0.5 hPa intervals) and temperature (shading), corrected to sea level assuming the dry adiabatic lapse rate) at 1300 UTC 17 October 2011 from the 1.5 km model. "L" denotes the centre of the frontal wave. Met Office surface temperature observations (coloured circles) and wind observations (white barbs) at 1200 UTC 17 October 2011 are overlaid for comparison. Temperature circles use the same colour scale as for the model temperatures. Wind barbs are plotted using standard notation (one full barb for every 10 knots of wind speed, and half a barb for five knots, with open circles indicating calm conditions) [Colour figure can be viewed at wileyonlinelibrary.com]

tornadoes. The location of the three tornado reports is shown by star symbols in Figure 3. The tornadoes occurred immediately down-front of the wave centre, during the early stages of development when the wave was deepening rapidly, and where p[TN] was increasing rapidly.

3.3 | Wave development in the 1.5 km model

The structure and evolution of the frontal wave may be analysed in more detail using output from the 1.5 km model. At 1300 UTC, the wave is centred over the Irish Sea between Northern Ireland and southwest Scotland (Figure 4). The frontal boundary is well-defined, marked by a sharp mean-sea-level pressure (MSLP) trough and a large vector wind difference across the trough axis, with associated strong cyclonic vertical vorticity and horizontal convergence. Coincident with this shear zone is a similarly narrow and well-defined baroclinic zone, across which temperatures typically differ by 4–5 °C and locally as much as 6–7 °C. Observations and model data show that the frontal boundary was narrow and well-defined both up-front and down-front of the wave centre at this time (e.g. note the large wind direction and temperature differences across the front over both southern Scotland and Ireland in Figure 4), demonstrating that the trailing

front had already collapsed to narrow cross-frontal scales (Hoskins and Bretherton, 1972) by the early stages of secondary cyclogenesis. This characteristic probably relates to the antecedent conditions; specifically, the substantial resultant deformation, in which the axis of dilatation was orientated at a small angle to the front, before and during the early stages of wave development (Figure 2). This is consistent with the analysed positive frontogenesis along the full length of the front in the early stages of development (Figure 3d). The presence of such a "pre-existing" narrow frontal shear zone was postulated by CP20 to be a key feature in tornadic frontal waves, since modulation of the along-front distribution of shear vorticity and stretching deformation during the early stages of wave development can only result in shear-zone vortex-genesis if the shear zone is already narrow and well-defined in these early developmental stages.

Figure 5 illustrates the evolution of the wave in the 1.5 km model between 1200 and 2200 UTC 17 October. The wave centre is marked by a local MSLP minimum, initially elongated in the along-front direction, and a corresponding local vertical vorticity maximum along the shear zone (e.g. as over Ireland in Figure 5a).[5] As the wave moves northeast and matures, the pressure minimum becomes more circular and the largest values of vertical vorticity along the shear zone migrate towards the northern flank of the MSLP minimum. At the same time, a local along-front *minimum* in shear zone vertical vorticity develops immediately down-front of the wave centre (as shown by the break in the narrow zone of vertical vorticity $>1 \times 10^{-3}$ s^{-1} (yellow shading) along the front in this region in Figure 5f), which is associated with the onset of frontal fracture (Shapiro and Keyser, 1990). The wave's central pressure decreases by 17 hPa over the 10 hr period ending 2200 UTC, due to a combination of pressure falls following the wave centre (i.e. genuine deepening of the wave) and translation of the wave towards lower background values of MSLP (i.e. up-front translation within the cyclonic pressure field associated with the primary cyclone). The modelled location of the wave centre, and values of central pressure at 1200 and 1800 UTC, agree very closely with the analysed locations and central pressures at the same times (e.g. cf. Figure 1b,c), suggesting that the 1.5 km model has an accurate representation of the wave's location, track, and rate of development. However, down-front of the wave centre, the south-eastward movement of the NCFR across the United Kingdom was slightly too slow, with frontal

---

[5]In the calculation of these vorticity fields, the wind field has been averaged over nine grid boxes in the x and y directions in order to smooth out some of the very small-scale variability along the shear zone. This small-scale variability is subsequently analysed in more detail using unsmoothed fields.
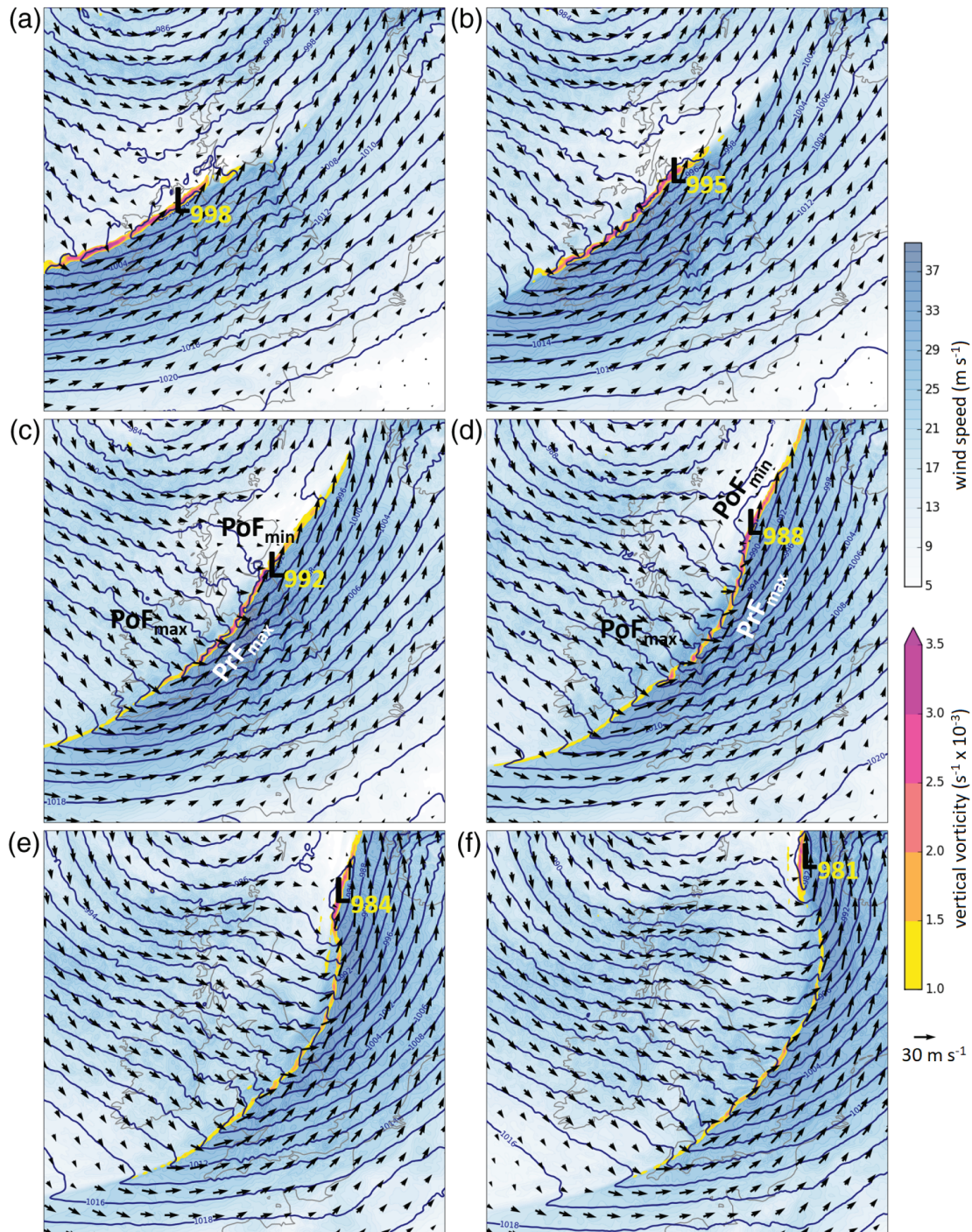
FIGURE 5 Wind vectors (arrows), MSLP (navy-blue contours at 2 hPa intervals), wind speed (blue shading), and vertical vorticity (over-plotted, yellow–pink shading) at 845 m AGL from the 1.5 km model, showing evolution of the frontal wave at (a) 1200 UTC; (b) 1400 UTC; (c) 1600 UTC; (d) 1800 UTC; (e) 2000 UTC; (f) 2200 UTC 17 October 2011. Parameter fields have been smoothed by averaging over 9 × 9 grid boxes at the 1.5 km native model grid spacing. "L" denotes the centre of the frontal wave at each time, with the central pressure (hPa) annotated. Additional annotations in (c,d) highlight various features of the flow pattern characteristic of frontal waves of the type described by CP20: a local minimum in wind speed and MSLP gradient on the cold side of the front near and immediately up-front of the frontal wave's centre (PoF_{min}); a local maximum in wind speed and pressure gradient on the cold side of the front, down-front of the wave centre (PoF_{max} in (d)), in which winds are orientated nearly normal to the front and point towards the front (i.e. a maximum in $-v'_{cold}$); a local maximum in wind speed and MSLP gradient on the warm side of the front, near and down-front of the wave centre (PrF_{max} in (d)), in which winds are orientated nearly parallel to the front. In the system-relative frame of reference, PrF_{max} constitutes part of the cyclone's warm conveyor-belt flow (Harrold, 1973) [Colour figure can be viewed at wileyonlinelibrary.com]
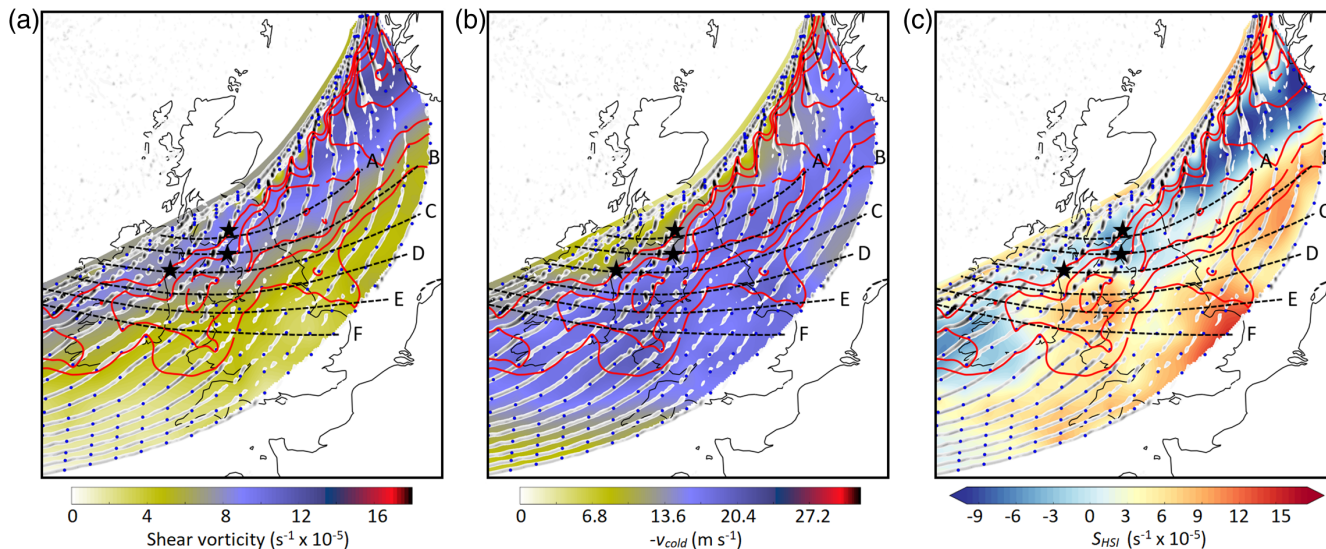
FIGURE 6 Bulk parameter fields analysed at 1,390 m AGL (∼850 hPa) from the 1.5 km model, derived by interpolation of bulk values at along-front points every hour over the period 1000 UTC 17 October – 0000 UTC 18 October 2011. (a) Shear vorticity; (b) $-v'_{cold}$; (c) Dritschel *et al.* (1991) criterion for the growth of vortices by HSI (S_{HSI}). Overplotted grey shading shows smoothed vertical vorticity at 75 m AGL, showing the location of the frontal shear zone at each hour; individual on-front analysis points are shown by blue dots. Red contours show p[TN] at intervals of 0.1, starting at 0.5. Black dashed lines show the tracks of selected perturbations along the shear zone (labelled A – F). Black star symbols denote the locations of reported tornadoes [Colour figure can be viewed at wileyonlinelibrary.com]

passage in the model occurring ∼1 hr later than observed in most places.

Figure 6 illustrates the spatio-temporal distribution of bulk shear vorticity, $-v'_{cold}$ and S_{HSI} over the period 1000 UTC 17 October – 0000 UTC 18 October 2011, as constructed from hourly 1.5 km model wind fields at 1,390 m AGL. Substantial variability is evident in the selected parameter values as the developing frontal wave moves across Ireland and the United Kingdom. In agreement with the ERAi values (Figure 3), shear vorticity is maximised close to the wave apex and increases steadily as the wave amplifies (i.e. from southwest to northeast along the wave's track; Figure 6a). The parameter $-v'_{cold}$ is maximised down-front of the wave, along a broad zone that tracks through southern Ireland, Wales and much of England, but remains much smaller north of the wave centre (Figure 6b). p[TN] (red contours in Figure 6) is maximised just down-front of the shear vorticity maximum and just up-front of the $-v'_{cold}$ maximum; a swath of p[TN] > 0.5 extends from ∼50 to ∼250 km down-front of the wave centre, with peak values increasing gradually along the track of the wave. S_{HSI} is positive in most places along the front (suggesting an environment generally unfavourable for the development of vortices by the release of HSI), with values reaching a maximum where $-v'_{cold}$ is large, near the centre of the meso-α-scale frontal bulge, and in a separate region immediately up-front of the wave centre (Figure 6c). Between these regions, a minimum in S_{HSI} is evident, with values slowly decreasing as the wave

develops. $S_{HSI} < 0$ (suggesting an environment favourable for the growth of vortices by HSI) occurs within a narrow swath immediately down-front of the wave centre (Figure 6c), appearing first over Northern Ireland and then tracking northeast close to the England–Scotland border, before moving into the North Sea.[6] The reported tornadoes (black star symbols in Figure 6) occur within this S_{HSI} minimum. The reduced S_{HSI} in this region corresponds to reducing bulk confluence (not shown) and contemporaneous increasing shear vorticity. Bulk diffluence eventually develops near the wave centre by the time the wave reaches maturity, consistent with transition to frontolysis along the same part of the front in the ERAi fields (Figure 3d). This transition is associated with the onset of frontal fracture (as described subsequently).

In summary, analysis of bulk measures from the 1.5 km model shows that the tornadoes occurred within a narrow strip where relatively large and increasing values of p[TN] coincide with negative S_{HSI}.

---

[6]$S_{HSI} < 0$ is also evident over and near southwest Ireland, and in the far southwestern corner of the analysis domain. The former region is associated with a separate, weak frontal wave (as suggested by the presence of a shallow inflection in the frontal shear zone over far southwest Ireland) which fails to amplify and eventually becomes subsumed into the main wave development over the United Kingdom. The latter is likely explained by the fact that the shear-zone depth is less than the 1,390 m analysis height along the trailing part of the cold front, far down-front of the frontal wave centre.

FIGURE 7 (a) Smoothed 75 m AGL vertical vorticity (colour shading) at hourly intervals from 0900 UTC 17 October to 0000 UTC 18 October 2011 from the 1.5 km model. Dashed lines show the tracks of selected vortices along the frontal shear zone, labelled A – F. (b) Smoothed 75 m AGL vertical vorticity from the 1.5 km model at 1600 UTC 17 October 2011 (colour shading). The section of front exhibiting substantial meso-γ-scale perturbations is highlighted by blue shading. "L" denotes the modelled location of the wave centre [Colour figure can be viewed at wileyonlinelibrary.com]
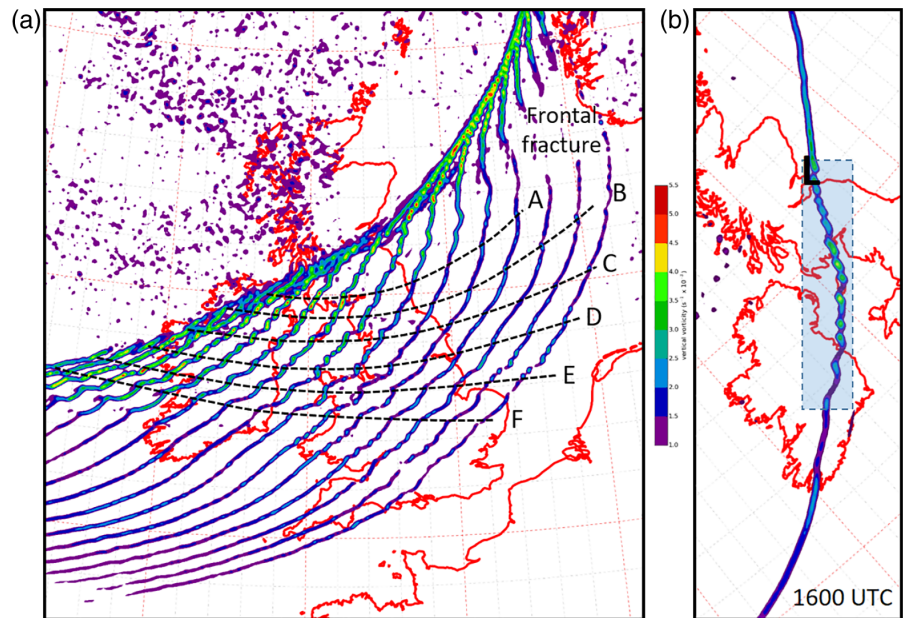
4 | VORTEX-GENESIS IN THE 1.5 KM MODEL

Having described the frontal wave development and associated spatio-temporal evolution of key environmental parameters, we now focus on the details of primary vortex-genesis and evolution in the 1.5 km model, identifying preferred regions for vortex-genesis. Figure 7a shows 75 m AGL vertical vorticity along the frontal shear zone at hourly intervals between 1000 and 2300 UTC 17 October 2011 from the 1.5 km model. Local perturbations in the shear zone, which are associated with the genesis and subsequent amplification of primary, meso-γ-scale vortices, are evident close to the wave centre and along the meso-α-scale frontal bulge, tracking through the Irish Sea and much of northern England and southern Scotland. The preferential development of vortices along this part of the front is best appreciated when inspecting vertical vorticity fields at individual analysis times, especially in the early stages of wave development (e.g. Figure 7b). A marked absence of similar perturbations is noted both up-front of the wave centre, and along the trailing part of the front, far down-front of the wave centre, where the shear zone instead appears highly two-dimensional.[7] The section of the front exhibiting meso-γ-scale perturbations is therefore well-defined, bounded both up-front and down-front by a shear zone exhibiting a comparative absence of such structures.

The tracks of individual vortices and associated perturbations may be determined by inspection of vertical vorticity at the lowest model level at 5 min intervals throughout the analysis period (not shown). Tracks of selected vortices are shown by dashed lines in Figure 7. In each case, the vortices originate as subtle vertical vorticity maxima along the shear zone, with associated small-amplitude perturbations developing soon after genesis. Over a period of several hours, the associated perturbations amplify whilst moving down-front relative to the wave centre. New vortices continue to develop near the wave centre, such that the along-front extent of the region with substantial perturbations increases with time. The tracks of individual perturbations diverge slightly, being orientated southwest–northeast over northern England and Scotland, compared to west–east or even west-northwest–east-southeast over central and southern England. The orientation of perturbation tracks, and its variability across the domain, agrees well with the tracks of the larger radar-observed perturbations in the real NCFR (Figure 8).

The apparent up-front movement of the wave relative to individual vortices and associated perturbations is explained by the differing along-front velocity components of the wave and the vortices. Relative to the front-normal direction, both the frontal wave and the individual vortices move up-front; however, the up-front movement of the wave is greater than that of individual vortices, with the consequence that individual vortices move down-front *relative to the wave*. The observed coupling between the wave centre and the 300 hPa PV maximum after ~1200 UTC (Figure 1b–d) suggests that the along-front movement of the wave is controlled by the velocity of the driving

---

[7]More detailed analysis of unsmoothed fields (not shown) reveals that the front is not entirely two-dimensional in these regions. However, perturbations are comparatively small, transient, and show limited up-scale growth.
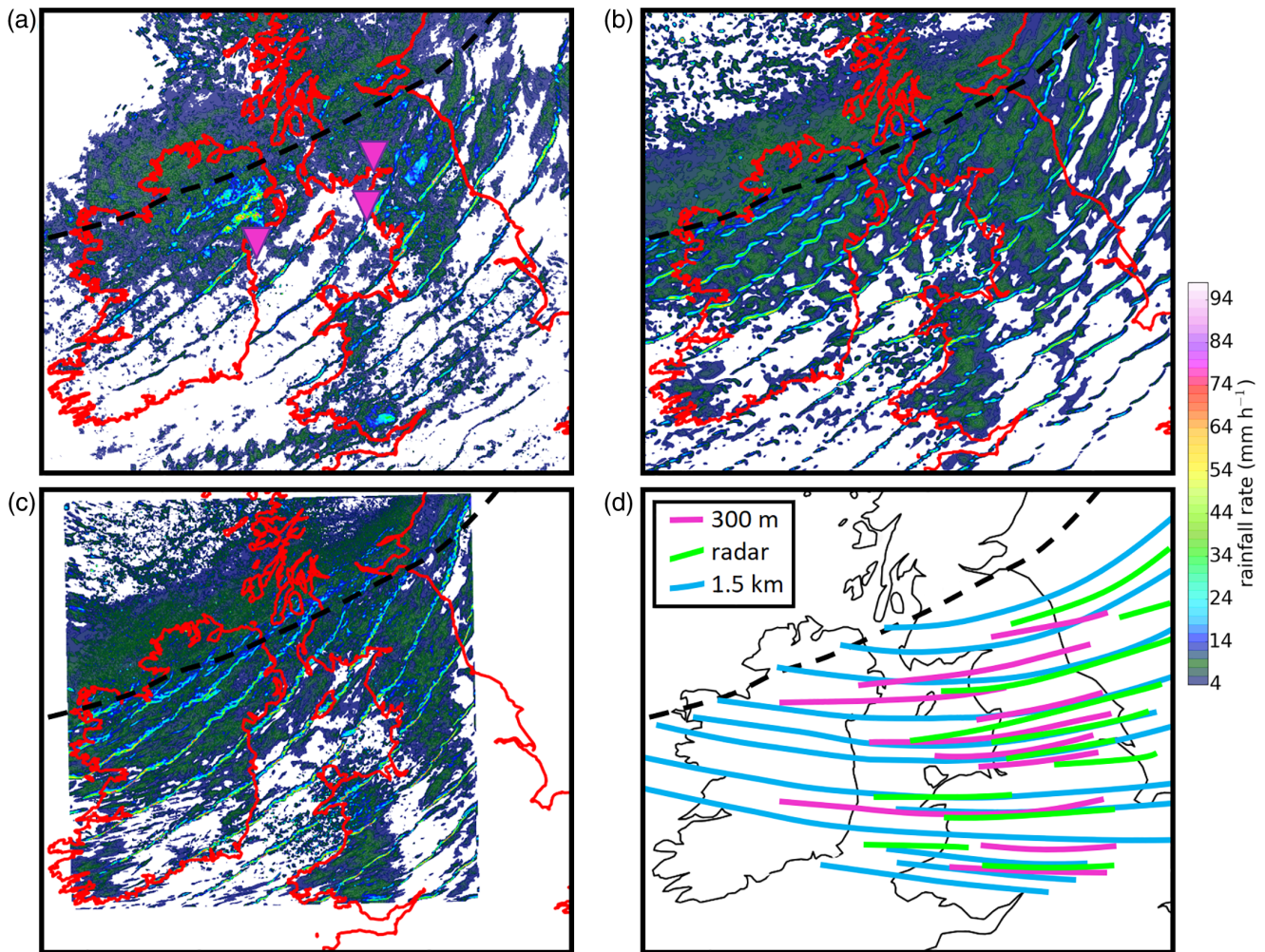
FIGURE 8 Comparison of instantaneous rainfall rates (mm·hr⁻¹) (composited at hourly intervals over the period 1000 UTC 17 October to 0000 UTC 18 October 2011) from (a) the UK and Ireland radar network; (b) the 1.5 km model; and (c) the 300 m model. The track of the modelled wave centre is shown by the bold, dashed line in each panel. (d) Tracks of prominent NCFR inflections and/or gaps in the radar data and the 1.5 km and 300 m model rainfall rate fields. Magenta inverted triangles in (a) show the location of tornado reports [Colour figure can be viewed at wileyonlinelibrary.com]

upper-level PV maximum, whilst the along-front velocity of shear-zone vortices is likely controlled by the mean of the along-front wind component on each side of the shear zone, as previously suggested for vortices forming along NCFRs and other types of boundary (e.g. Parsons and Hobbs, 1983; Adlerman and Droegemeier, 2005).[8]

The wave-relative movement of vortices and the ongoing development of the frontal wave results in substantial Lagrangian changes in the bulk environmental parameters following individual vortices (hereafter "pseudo-Lagrangian", since individual air parcels are not followed as in a true Lagrangian frame of reference), as depicted for selected vortices by the bold coloured lines in Figure 9. To provide a more complete

picture of the evolution, values are plotted from 0800 UTC, which is approximately 5, 3 and 2 hr prior to vortex-genesis for vortices A, B and C, respectively. Prior to vortex-genesis, local values are analysed at the point where the backward-extrapolated vortex track intersects the shear zone at each analysis time. In practice, since the FNFM is very small up-front of the wave centre, and because vortex-genesis occurs near to the wave centre in each case, the backward-extrapolated positions generally lie very close to the actual location of vortex-genesis. The evolution of environmental parameters is therefore analysed over the period that the frontal wave centre approaches, passes and then recedes up-front of each pseudo-Lagrangian analysis point.

At all points, p[TN] is initially small, but increases markedly as the frontal wave centre approaches and passes (Figure 9a,b; recalling that the frontal wave moves up-front faster than individual vortices along the shear

---

[8]This behaviour also arises in basic treatments of Kelvin–Holmholtz type instabilities (e.g. Kundu and Cohen, 2004; p. 489).
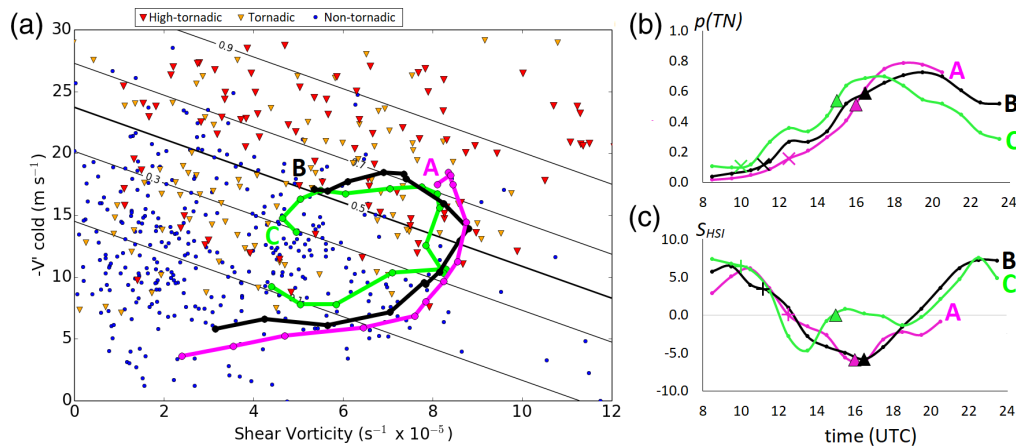
FIGURE 9   (a) Scatterplot of shear vorticity versus $-v'_{cold}$ for high-tornadic, tornadic and non-tornadic analysis points (red, orange and blue markers, respectively) from the dataset analysed in CP20. Black contours denote the probability of a point being tornadic or high-tornadic across the two-dimensional parameter space (i.e. $p[TN]$), which is calculated using linear discriminant analysis (see CP20 for details). Bold, coloured lines show the temporal evolution of smoothed 1,390 m AGL shear vorticity and $-v'_{cold}$ for three vortices (A, B and C) in the 1.5 km model (see Figure 7 for the tracks of these vortices). Values are computed every hour, by linear interpolation along the front where the vortex lies between on-front analysis points. Values are also averaged over two consecutive hours, then plotted at the half hour between (e.g. 1000 and 1100 UTC values averaged and plotted at 1030 UTC), to reduce the impact of noise in the individual hourly values. (b,c) Time series (hr) of $p[TN]$ and S_{HSI} at the locations of the same vortices over the period 0800 UTC 17 October – 0000 UTC 18 October 2011, again analysed at 1,390 m AGL using 1.5 km model data. Triangles denote the time of closest passage of each vortex to a reported tornado. Cross symbols denote the approximate time of passage of the frontal wave centre [Colour figure can be viewed at wileyonlinelibrary.com]

zone). Transition to large $p[TN]$ occurs earliest at the pseudo-Lagrangian point of vortex C (hereafter point C), since the frontal wave centre is already close to this point at 0800 UTC, and latest at the pseudo-Lagrangian point of vortex A, which is located furthest up-front and therefore experiences later passage of the wave centre. The particularly low initial values of $p[TN]$ at point A are representative of the environment ~200–300 km up-front of the wave centre. In the two-dimensional parameter space defined by shear vorticity and $-v'_{cold}$, traces for each vortex follow a curve, since shear vorticity and $-v'_{cold}$ increases occur at different times (i.e. in different locations relative to the wave centre). Initially, as the wave centre approaches, shear vorticity increases whilst $-v'_{cold}$ remains small. As the wave centre passes, shear vorticity reaches a peak and a rapid increase in $-v'_{cold}$ ensues, with FNFM correspondingly beginning to increase. As the wave centre recedes up-front of the vortex, shear vorticity begins to decrease whilst $-v'_{cold}$ and FNFM continue to increase slowly, reaching a maximum as PoF_{max} (Figure 5c,d) approaches and then passes each pseudo-Lagrangian point. Thereafter, both parameter values begin to decrease as the wave recedes further up-front.

The period of large $p[TN]$ is seen to be transitory, with values greater than 0.5 lasting only ~6–10 hr at each point (vortex A ends up in the frontal fracture region, and therefore dissipates whilst $p[TN]$ is still large; however, even here, values are beginning to decrease by the time

the vortex dissipates). The time of closest passage of each vortex to a reported tornado is shown by the triangle symbols in Figure 9b. Tornadoes occurred during the period of rapidly increasing $p[TN]$, rather than at the time of maximum $p[TN]$. This characteristic was also found for the frontal wave case of 1 January 2005 by CP20, suggesting that tornado-genesis may be more closely related to Lagrangian trends in $p[TN]$ than its absolute value at any instant in time.

Evolution of the local environment of vortices A, B and C may also be described in terms of S_{HSI} (Figure 9c). In all cases, a transition from conditions unfavourable for the growth of vortices by the release of HSI (i.e. $S_{HSI} > 0$) to conditions favourable for such growth (i.e. $S_{HSI} < 0$) occurs around or just after the time of wave passage, which corresponds closely to the time of vortex-genesis. In vortices B and C, the transition to $S_{HSI} < 0$ is temporary, however, with a recovery to positive values as the wave recedes further up-front. In vortex A, values remain negative up to the time of vortex dissipation in the frontal fracture region. In all cases, the closest passage of the model vortex to a reported tornado in the real NCFR occurs close to or just after the time of minimum S_{HSI}.

In summary, the 1.5 km simulation shows that primary vortices develop preferentially near to the centre of the frontal wave in the early stages of wave development, with individual vortices moving down-front of the wave centre with time. The genesis of vortices is apparently
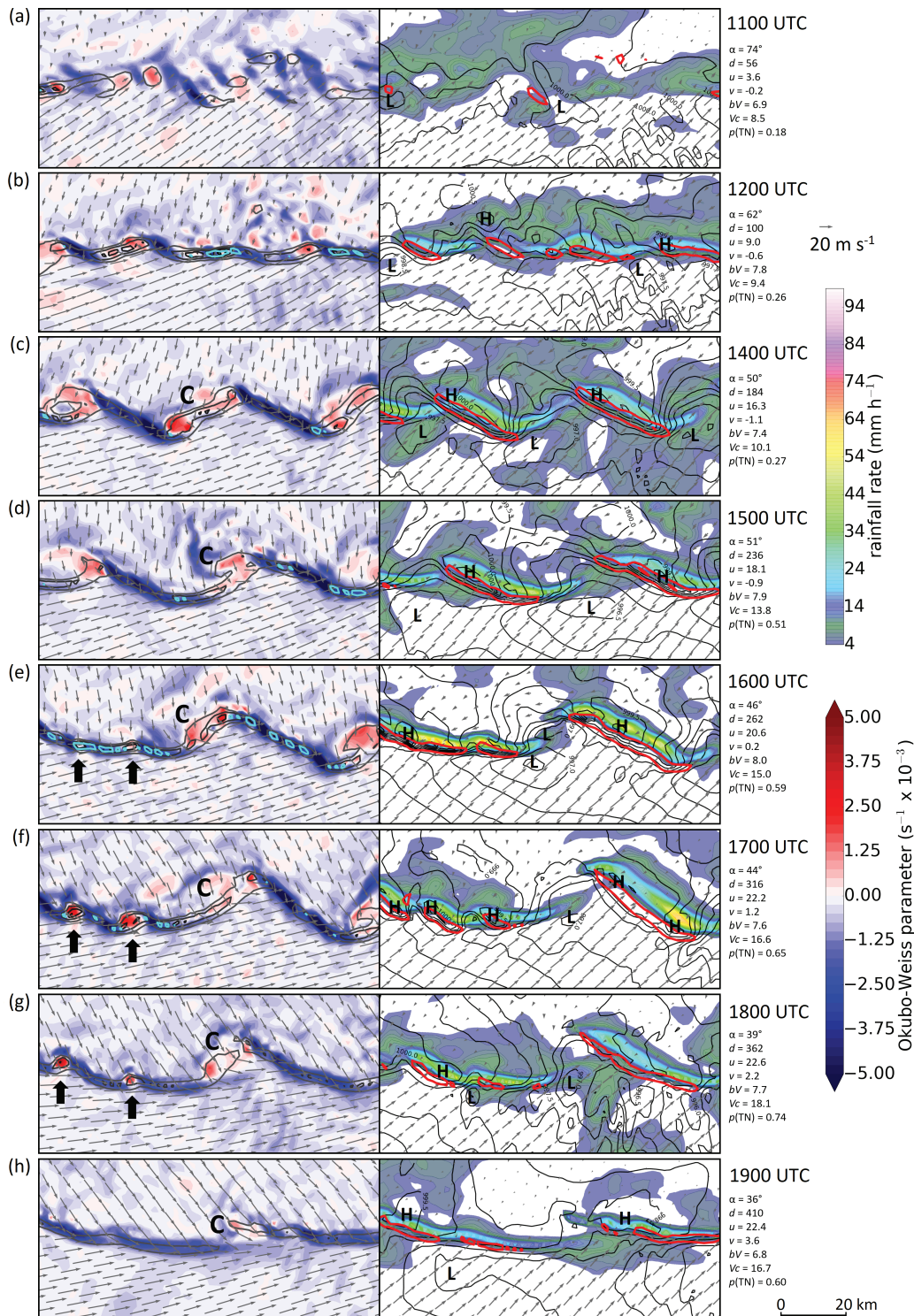
FIGURE 10 Evolution of MSLP, rainfall rate and 555 m AGL wind fields near vortex C (as labelled) over the period 1100–1900 UTC 17 October 2011 from the 1.5 km model. Left column: Okubo–Weiss parameter (shading), vertical vorticity (grey-black contours; contour interval 3×10^{-3} s^{-1} starting at 3×10^{-3} s^{-1}), ground-relative wind vectors (arrows, plotted every 4.5 km in the x and y directions). Cyan contours enclose regions with vertical vorticity stretching $>2 \times 10^{-4}$ s^{-2}. Bold arrows in (e–g) denote locations of secondary vortices. Right column: rainfall rate (colour shading), vortex-relative wind vectors (arrows), MSLP (solid contours at 0.5 hPa intervals) and horizontal convergence (bold, red contours at intervals of 2×10^{-2} s^{-1}). "L" and "H" denote local MSLP minima and maxima, respectively. The domain shown has width 100 km and is rotated such that the x-axis is parallel to the local front at all times. Figures to the right of the panels indicate the local orientation of the front (α, degrees clockwise of a north–south line), down-front distance of domain centre from the frontal wave centre (d, km), x and y components of the vortex translational velocity (u, v, m·s^{-1}), shear vorticity (bV, s$^{-1} \times 10^{-5}$), $-v'_{\text{cold}}$ (Vc, m·s^{-1}), and p[TN]. The latter three parameters are computed from the interpolated fields shown in Figure 6 [Colour figure can be viewed at wileyonlinelibrary.com]
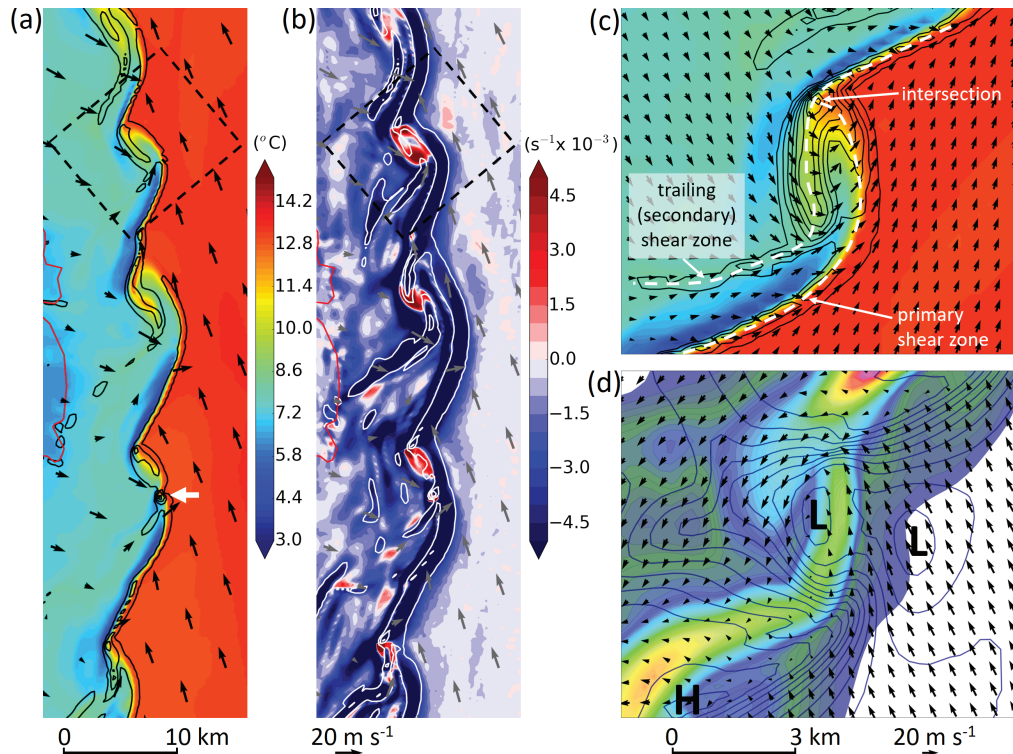
FIGURE 11   Primary vortices over the Irish Sea just to the east of Northern Ireland at 1500 UTC, from the 300 m model. (a) Surface temperature (colour shading), 10 m AGL vertical vorticity (black contours at intervals of 1.6×10^{-2} s^{-1}, starting at 0.4×10^{-2} s^{-1}) and wind vectors (arrows, plotted every 4.5 km in the x and y directions). (b) Okubo–Weiss parameter (colour shading), 10 m AGL horizontal convergence (white contours at intervals of 1.6×10^{-2} s^{-1}, starting at 0.4×10^{-2} s^{-1}) and wind vectors (arrows). Panels are rotated such that the y-axis is parallel to the local front. The coastline of Northern Ireland is shown in red. (c,d) Closer view of one of the primary vortices over the area denoted in (a,b) by the dashed boxes. (c) Surface temperature (colour shading; scale as in (a)), ground-relative wind vectors (arrows, plotted every 0.6 km in the x and y directions) and vertical vorticity (black contours at intervals of 0.4×10^{-2} s^{-1}, starting at 0.2×10^{-2} s^{-1}). (d) Rainfall rate (colour shading; scale as in Figure 10), vortex-relative wind vectors (arrows) and MSLP (navy-blue contours at intervals of 0.3 hPa) [Colour figure can be viewed at wileyonlinelibrary.com]

orchestrated by the associated spatio-temporal variations in relevant environmental parameters. Vortex-genesis ceases as the frontal wave matures, due to onset of frontal fracture and associated dissipation of a well-defined shear zone in the high p[TN] region. The wave-relative location of vortex-genesis in the model is consistent with the observed location and timing of reported tornadoes in the real NCFR.

5 | EVOLUTION OF A PRIMARY VORTEX IN THE 1.5 KM MODEL

Using output from the 1.5 km simulation, we now explore in more detail the evolution of the shear zone near to primary vortex C (Figure 10; see Figure 7 for the location and track of this vortex). We describe how the relative movement up-front of the frontal wave impacts upon the local structure of the wind field near the NCFR, the evolution of the shear zone, and the timing of vortex-genesis. The influence of the vortex on the meso-γ-scale structure of the

NCFR, which is later compared with radar observations of the real NCFR, is also explored throughout the life cycle of the vortex. The morphology and evolution of vortex C is considered typical of the primary vortices in the 1.5 km simulation. The domain moves with the travelling shear zone and the centre is fixed near the vortex for all analysis times.

At the outset (Figure 10a), the domain is situated just up-front of the wave centre. The shear zone is already reasonably well-defined, with an abrupt decrease in wind speed across the frontal boundary (the area of light winds post-front is part of the region marked $PoF_{\min}$ in Figure 5). An area of stronger, forward-directed flow is evident further rearward of the front (towards the top-left corner of the panels in Figure 10a), which catches up with the shear zone as the centre of the frontal wave passes through the domain (cf. Figure 10a,b). Horizontal convergence and vertical vorticity consequently increase substantially, with associated narrowing of the shear zone. A well-developed NCFR forms by 1200 UTC, with local rainfall maxima
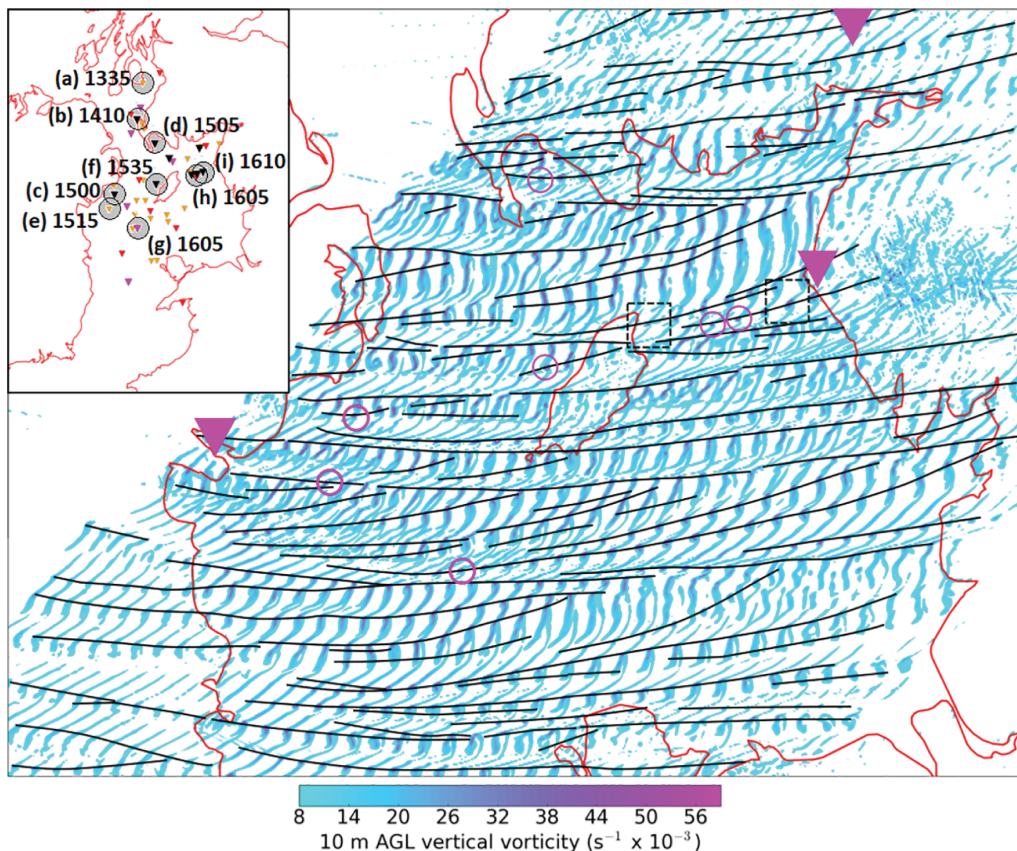
FIGURE 12 Relative vertical vorticity at 10 m AGL (colour shading) at 5 min intervals over the period 1435–1755 UTC 17 October 2011 from the 300 m model. Black lines show tracks of miso-scale vortices (subjectively analysed). Magenta circles highlight vortices having vertical vorticity $>7.5 \times 10^{-2}$ s^{-1}. Magenta inverted triangles are tornado reports. Small dashed boxes near the Isle of Man and Cumbria denote, respectively, the area shown in panels (a) and (g) of Figure 13. Inset panel: locations (inverted triangles) of 10 m AGL vertical vorticity stretching maxima exceeding 2.2×10^{-3} s^{-1} (orange), 2.4×10^{-3} s^{-1} (red), 2.6×10^{-3} s^{-1} (magenta) and 2.8×10^{-3} s^{-1} (black) from the 300 m model. Grey filled circles denote the locations of vorticity maxima $>7.5 \times 10^{-2}$ s^{-1}. Overlaid text indicates the time of occurrence of each (in UTC) and the letter indicates the corresponding panel in Figure 14 [Colour figure can be viewed at wileyonlinelibrary.com]

>30 mm·hr^{-1} (Figure 10b). Individual vortices begin to develop along the shear zone around this time.

Over the following 1–2 hr, localised NCFR perturbations develop as vortex C (and neighbouring vortices) continue to intensify. By 1400 UTC (Figure 10c), the perturbations are well defined and occur with fairly regular along-front spacing. Analysed over a larger domain, the mean spacing at this time is 37.9 km (range 31.6–44.3 km). Between the perturbation centres, clockwise-turned filaments (hereafter "braids") develop, along which the shear zone becomes particularly narrow under the influence of increased horizontal convergence. Conversely, convergence decreases near the perturbation centres. A positive correlation exists between the magnitude of near-surface horizontal convergence, 1 km AGL updraught speed (not shown) and surface precipitation rate (e.g. as evident in the right-hand panels in Figure 10c,d), such that development of the vortices and associated along-front variability in horizontal convergence results in transition of an initially relatively unbroken NCFR (Figure 10b) to one exhibiting

marked "core–gap" morphology (e.g. Figure 10d). The cores, with rainfall rates locally >50 mm·hr^{-1}, are located at the braids between primary vortices, where the updraught speeds are maximised, with NCFR gaps forming near the primary vortex centres. This core–gap morphology, and the clockwise orientation of individual cores relative to the mean orientation of the front, is consistent with numerous observations and modelling studies of NCFRs in the literature (e.g. James and Browning, 1979; Matejka *et al.*, 1980; Hobbs and Persson, 1982; Parsons and Hobbs, 1983; Browning and Reynolds, 1994; Browning and Golding, 1995; Jorgensen *et al.*, 2003; Kawashima, 2007; Smart and Browning, 2009; Clark and Parker, 2014).

Over time, vertical vorticity at the braids increases as the shear zone narrows (e.g. immediately down-front of vortex C from 1400 to 1600 UTC; Figure 10c–e), and secondary vortices begin to develop in places, as shown by the presence of local vertical vorticity maxima with diameter ~3–4 km (marked by arrows in Figure 10e–g). In the 1.5 km model, these secondary vortices fail to exhibit

TABLE 1 Properties of the seven strongest secondary vortices (where strength is taken to be the maximum 10 m AGL vertical vorticity along the vortex track in the 5 min fields) in the 300 m simulation (for locations of these vortices, see inset panel of Figure 12)

Time of maximum vertical vorticity (UTC)	Max. Vertical vorticity (s^{-1} × 10^{-2})	Max. Vorticity stretching (s^{-2} × 10^{-3})	Max pressure deficit (hPa)	Max. Wind speed (m s^{-1})	Max. Differential velocity (m·s^{-1})	Diameter (km)	Translational velocity (m·s^{-1}, degrees)	Position of vorticity stretching max.
1410	8.29	2.97	0.9	28.3	23.4	1.53	17.3, 264	Collocated
1500	8.79	3.64	0.7	31.2	22.2	1.90	20.7, 264	W
1505	9.35	4.38	3.1	30.6	24.9	1.80	19.2, 270	NE
1515	7.73	2.40	−0.4	24.8	20.4	1.23	20.1, 275	N
1535	9.04	3.71	3.5	34.8	27.7	0.95	23.0, 244	N
1605	7.63	2.77	0.6	30.1	22.7	1.50	23.6, 262	N
1605	7.79	3.00	1.1	34.4	23.3	2.12	23.2, 259	NW
Mean	**8.37**	**3.27**	**1.4**	**30.6**	**23.5**	**1.58**	**21.0, 263**	**NNW**

Note: Pressure deficit is relative to the local MSLP on the immediate warm side of the front, outside of the vortex circulation. Diameter is that at the time of maximum differential velocity. Position of vertical vorticity stretching maximum is relative to the centre of the MSLP minimum at the time of maximum vertical vorticity. Maximum wind speed, and all wind derivatives, are analysed at the 10 m AGL level.

upscale growth and decay slowly after ~1700 UTC, disappearing entirely by 1900 UTC (cf. Figure 10f–h). Consequently, the secondary vortices have little impact on the overall structure and evolution of the NCFR. In contrast, the secondary vortices are apparently better resolved in the 300 m simulation, and become important in the evolution of the NCFR, as described subsequently.

From ~1700 UTC vortex C begins to dissipate, as shown by a weakening and eventual loss of the local MSLP minimum and circulation centre near the vortex centre (cf. Figure 10f,h) and an associated reduction in local values of the Okubo–Weiss parameter. However, a step-like break persists in the NCFR, associated with a local minimum in cross-frontal wind, temperature and MSLP gradients (Figure 10h). Inspection of the precipitation rates over the full model domain, and comparison with radar data (e.g. as in Figure 8), shows that these residual NCFR breaks may persist for several hours after the dissipation of the vortices originally responsible for their development.

6 | VORTEX-GENESIS AND EVOLUTION IN THE 300M SIMULATION

Having described the genesis and evolution of primary vortices in the 1.5 km simulation, we now compare these findings with output from the 300 m simulation. We focus on the secondary, miso-scale vortices and their impact on the NCFR structure and evolution, comparing with radar observations of the real NCFR. Motivating this analysis is a desire for improved operational recognition of the radar signatures associated with rapidly developing secondary vortices, which we suggest are preferred locations for tornadogenesis (i.e. the secondary vortices constitute possible NCFR tornado parent vortices).

6.1 | Comparison with 1.5 km simulation

On the scale of the frontal wave, the 300 m and 1.5 km simulations are similar, with both having the meso-α-scale NCFR bulge down-front of the wave centre over the Irish Sea, and evidence of long-lived meso-γ-scale NCFR perturbations associated with primary vortices and their remnants. Although structurally similar, the individual shear zone perturbations are smaller in the 300 m simulation and have smaller along-front spacing (cf. Figure 8b,c). A similar tendency for the size of various features to decrease with decreasing model grid-length has been noted in previous modelling studies; for example, in simulations of frontal rain bands (e.g. Harvey *et al.*, 2017), convective cells (Hanley *et al.*, 2015) and individual updraughts (Nicol *et al.*, 2015). In this respect, the 300 m model is closer to the radar observations in the current case (cf. Figure 8a). Another noticeable difference is that there is a much greater propensity for secondary vortex-genesis along the braid regions between existing vortices in the 300 m simulation. We suggest this is because the secondary vortices are better resolved in the 300 m simulation, though we cannot rule out the possibility that the increased vortex-genesis results from numerical noise (e.g. Dahl, 2020). Unlike in the 1.5 km simulation, most of these secondaries exhibit marked evolution and up-scale growth.

6.2 | NCFR and shear-zone structure prior to secondary vortex-genesis

Figure 11 shows a row of mature, primary vortices at 1500 UTC, before onset of widespread secondary vortex-genesis. These vortices developed in a manner closely resembling the early evolutionary stages of vortex C in the 1.5 km
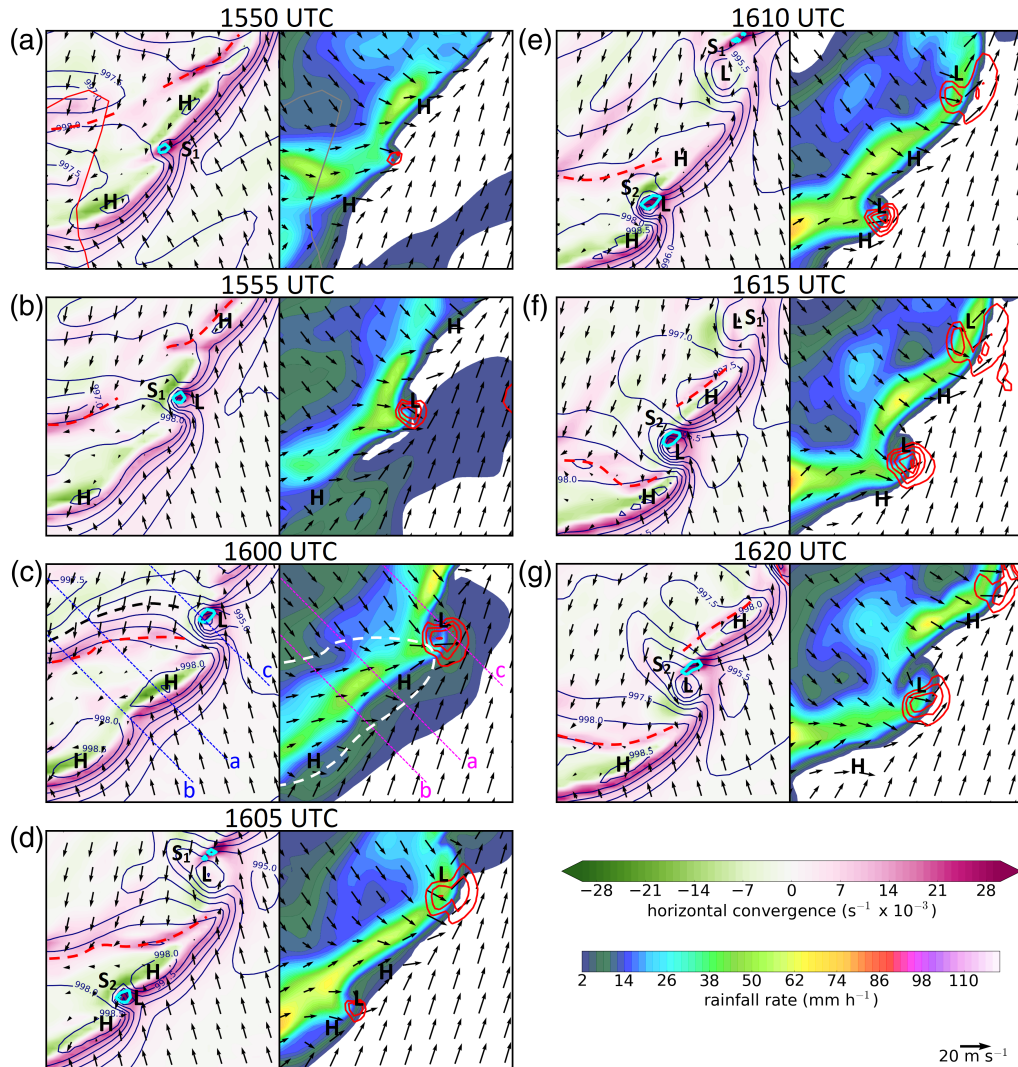
FIGURE 13 (a–g) Evolution of surface fields near selected secondary vortices (labelled S_1 and S_2) from the 300 m model. Left-hand panels: horizontal convergence (colour shading), vortex-relative wind vectors (arrows, plotted every 1.2 km), MSLP (navy-blue contours at 0.5 hPa intervals). Cyan contours enclose regions of vertical vorticity stretching $>1 \times 10^{-3}$ s^{-2}. Red, dashed lines denote the position of the secondary shear zone. Black, dashed line in (c) denotes position of an MSLP trough located behind the secondary shear zone. Right-hand panels: rainfall rate (colour shading), ground-relative wind vectors (arrows, plotted every 1.2 km) and wind speed (red contours at intervals of 2 m s^{-1}, starting at 26 m s^{-1}). White, dashed line in (c) encloses the region of southwesterly winds (and weak flow in the system-relative frame of reference) between the primary and secondary shear zones. Blue and magenta dashed lines in (c) denote the position of the vertical sections in Figure 15, with the adjacent letters indicating the corresponding panel number of Figure 15. Note that the northwest end of each vertical section lies beyond the edge of the domain shown here [Colour figure can be viewed at wileyonlinelibrary.com]

model (Figure 10a–d). The location of primary vortices is best seen by analysis of the Okubo–Weiss parameter, O, (Figure 11b), which is defined as the difference between the magnitudes of vertical vorticity and total horizontal strain (positive where vorticity exceeds strain: Okubo, 1970; Weiss, 1991).[9] Vorticity-dominant regions

$(O > 0$, denoted by red shading in Figure 11b) comprise discrete, well-defined centres that occur at regular intervals along the shear zone (mean spacing 14.2 km; range 11.0–17.4 km). In contrast, strain is dominant $(O < 0)$ along the braids. The mean spacing of primary vortices is just over one-third of that found in the 1.5 km model near to vortex C. We suggest the difference is symptomatic of the 1.5 km model's inability to simulate the true narrowness of the shear zone, given that linear theory predicts the growth rate to be maximised for perturbations of wavelength ~7.5 times the thickness of the shear zone (Miles and Howard, 1964).

---

[9]We use the definition of Schielicke *et al.* (2016) for the total horizontal strain, which comprises the sum of magnitudes of horizontal divergence, stretching deformation and shearing deformation. For clarity, we note that this differs from the Dritschel *et al.* (1991) horizontal strain, which comprises the stretching deformation only.

FIGURE 14 (a–i) Surface fields near the nine strongest vertical vorticity maxima (vertical vorticity $>7.5 \times 10^{-2}$ s^{-1}) in the 300 m model, centred on the vorticity maximum in each case. Rainfall rate (colour shading, scale as in Figure 10), vortex-relative wind vectors (arrows, plotted every 0.6 km), MSLP (navy-blue contours at 0.5 hPa intervals), wind speed (black contours at 2 m·s^{-1} intervals, starting at 24 m·s^{-1}) and vertical vorticity stretching (red contours at intervals of 0.8×10^{-3} s^{-2}) [Colour figure can be viewed at wileyonlinelibrary.com]
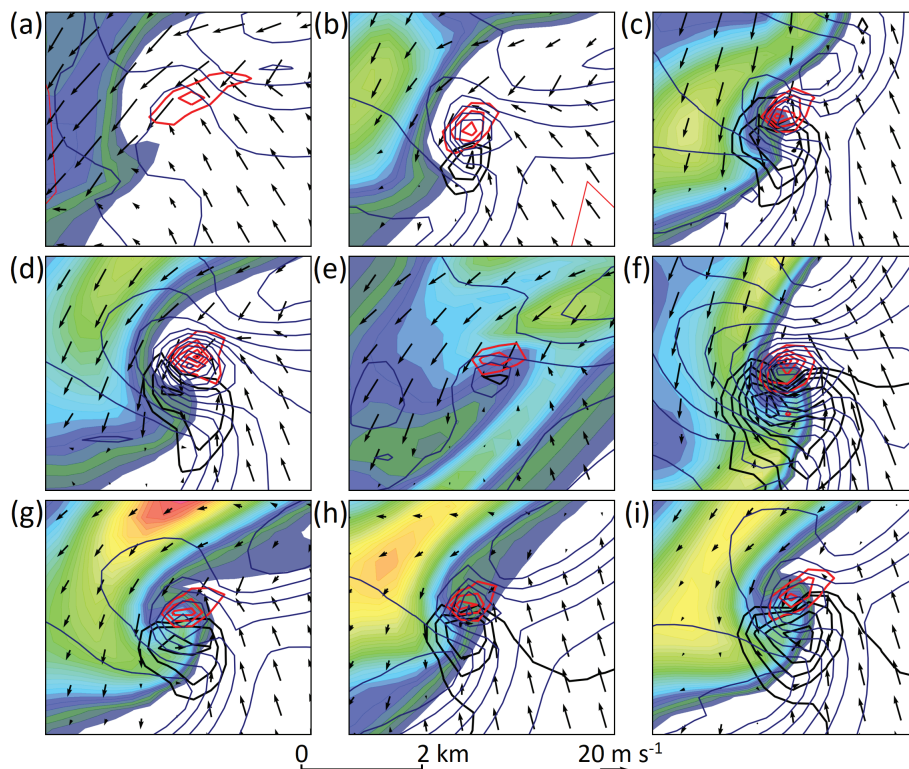
Near the primary vortices, the shear zone exhibits a complex structure; maxima in vertical vorticity generally occur along the flanks of the circulation centres, as noted in the 1.5 km simulation. A narrow filament of large vertical vorticity and relatively high temperatures is drawn out in the sheared flow on the rear flanks of each vortex (annotated in Figure 11c). Another elongated vertical vorticity maximum is drawn up-front on the forward flank of each vortex, intersecting the vorticity maximum along the braid region immediately up-front of the vortex (as annotated in Figure 11c). Secondary vortices in the 300 m simulation develop either along the braids, or near this intersection point of multiple shear zones on the flanks of primary vortices. An example of a strong secondary vortex at the shear zone intersection point on the flank of a primary vortex is highlighted by the white arrow in Figure 11a.

6.3 | Genesis and evolution of secondary vortices

After 1500 UTC, secondary vortex-genesis occurs in numerous places along the shear zone. Some idea of the variability in the development and evolution of vortices may be gained by inspection of vortex tracks, as inferred from 10 m AGL vertical vorticity fields at 5 min intervals between 1435 and 1755 UTC (Figure 12), during which period the cold front tracked across the Irish Sea (vortex tracks are analysed mainly over sea areas, because

topographical effects often complicate the near-surface vertical vorticity structure over land, which tends to obfuscate the analysis). The orientation of individual vortex tracks varies from west-northwest–east-southeast to southwest–northeast, sometimes over relatively small distances along the front. This reflects the variable tendency for secondary vortices to move towards and merge with the larger inflections associated with mature or decaying primary vortices. Over time it becomes impossible to distinguish between primary and secondary vortices, because many of the secondaries grow upscale to become the dominant feature along the local shear zone, whilst the primaries tend to become elongated in the along-front direction and ill-defined.

Detailed analysis of the development and evolution of individual secondary vortices is beyond the scope of the present article, but we summarise a few key findings (also see Table 1):

- The strongest secondary vortices (circled in Figure 12) exhibited 10 m AGL vertical vorticity $>7.5 \times 10^{-2}$ s^{-1} and generally occurred along the braids between primaries (rather than at shear-zone intersection points on the flanks of primaries).

- Most of these vortices occurred along the northern half of the meso-α-scale frontal bulge over the Irish Sea (i.e. just down-front of the frontal wave's centre). This corresponds closely to the region with tornado reports in the real NCFR, allowing for the land–sea issues alluded
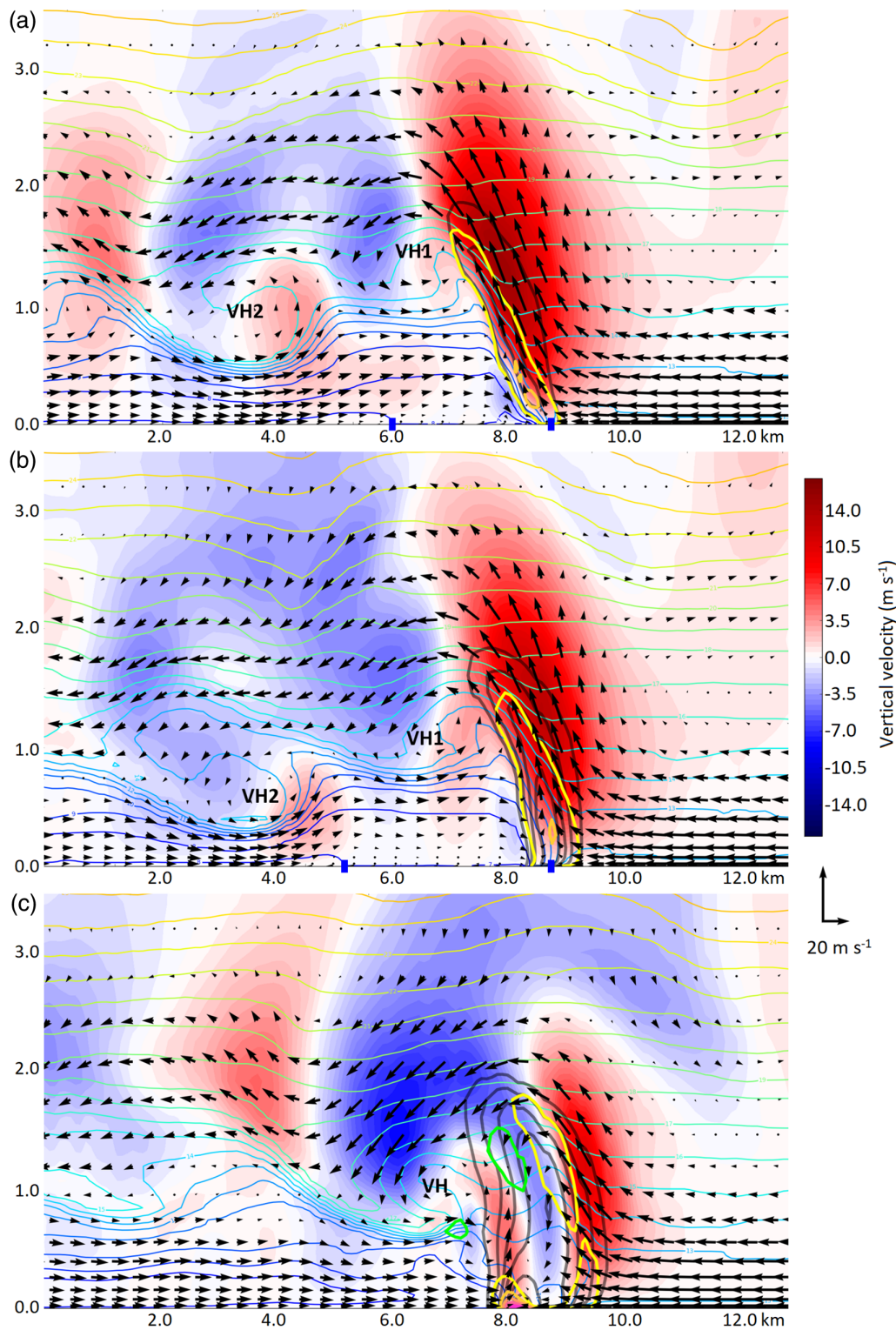
FIGURE 15 Vertical sections through the shear zone at 1600 UTC (see Figure 13c for the position of each) intersecting (a) the braid region between secondary vortices S_1 and S_2; (b) incipient vortex S_2; (c) mature vortex S_1. Vertical velocity (colour shading), θ (coloured contours at 1 K intervals), wind vectors parallel to the section (arrows, plotted every second model level in the vertical and every 0.36 km in the horizontal), vertical vorticity (grey contours at intervals of 1×10^{-2} s^{-1}), vertical vorticity stretching (yellow–pink contours at intervals of 4×10^{-4} s^{-2}, starting at 2×10^{-4} s^{-2}) and tilting of horizontal vorticity (lime contours at intervals of 4×10^{-4} s^{-2}, starting at 2×10^{-4} s^{-2}). "VH" indicates the location of horizontal vortices near the interface between the forward-relative and rearward-relative flows behind the surface front, as discussed in the main text. Blue markers on the x-axis in (a,b) denote the positions of the leading and trailing zones of horizontal shear [Colour figure can be viewed at wileyonlinelibrary.com]
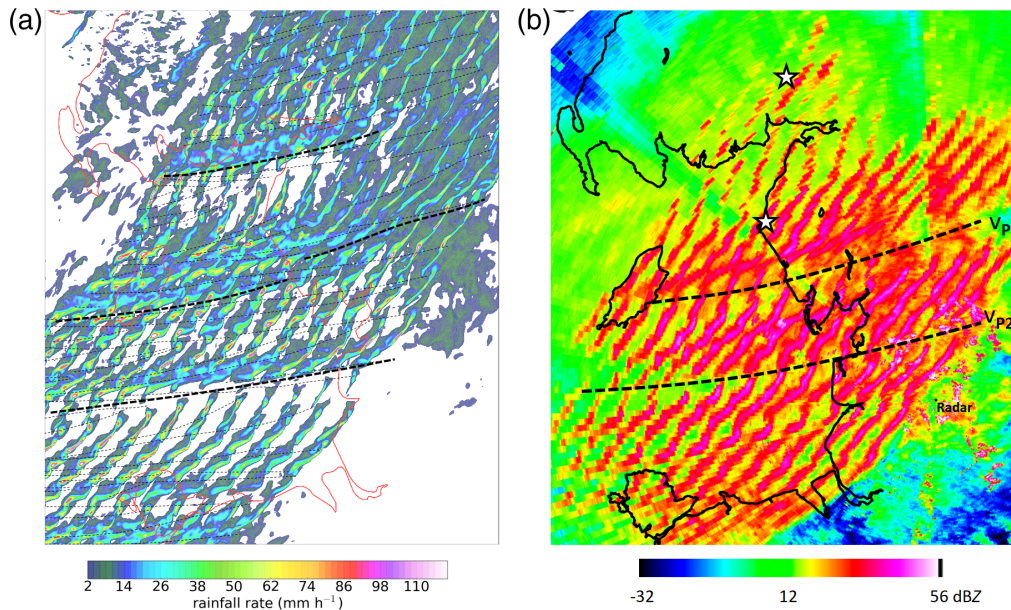
FIGURE 16 Comparison of (a) rainfall rate from the 300 m model and (b) raw reflectivity from the Hameldon Hill radar, showing evolution of the NCFR over northwest England and adjacent parts of the Irish Sea. Model data are plotted every 10 min over the period 1535–1755 UTC, and radar data every 10 min over the period 1500–1730 UTC. Tracks of larger NCFR inflections and gap regions are indicated by bold, dashed contours in each panel. Narrow, dashed contours in (a) are subjectively analysed tracks of shear-zone vorticity maxima (as in Figure 12). White stars in (b) denote the location of confirmed tornadoes [Colour figure can be viewed at wileyonlinelibrary.com]

to above (reported tornado locations are shown by the large magenta inverted triangles in Figure 12).

- These vortices developed extremely rapidly, amplifying from subtle inflections along the braids to maximum vertical vorticity, with an associated closed circulation in the 10 m AGL wind field, in 5–15 min (Figure 13).

- Vortices were associated with characteristic miso-scale perturbations in the NCFR, including small bulges, hooks or appendage echoes at the NCFR leading edge near the southern flanks of the vortices, and inflow notches near the northern flanks (Figure 14).[10] In the latter stages of vortex development, "broken-S" rainfall signatures (McAvoy *et al.*, 2000; Grumm and Glazewski, 2004; Lane and Moore, 2006) sometimes occurred, due to the development of a rainrate minimum near the vortex centre (as found for the primary vortices).

- The secondary vortices exhibited a core of $>25 \, \text{m·s}^{-1}$ ground-relative wind speeds on their southern flanks, where the rotational and background flow fields are additive, and a region of intense vertical vorticity stretching on their north or northwest flanks (Figure 14), where low-level ($<0.5 \, \text{km AGL}$) updraught speeds are maximised.

---

[10]In one case these features occurred near the rear edge of the NCFR (Figure 14e).

Vertical sections through selected vortices (Figure 15) reveal that the secondary vortices are relatively shallow (commensurate with the shallowness of the NCFR, more generally), with large vertical vorticity ($>1 \times 10^{-2} \, \text{s}^{-1}$) generally restricted to the lowest 2 km AGL; mature vortices exhibited a central downdraught with updraughts on both flanks of the vortex (e.g. Figure 15c). The intense vorticity stretching maximum on the north or northwest flank of the secondary vortices, which we suggest to be a preferred region for tornadogenesis, is evidently particularly shallow, with stretching $>2 \times 10^{-4} \, \text{s}^{-2}$ extending to only $\sim 250 \, \text{m AGL}$ (Figure 15c).

The vertical sections reveal that, at the scale of the secondary vortices, the shear zone exhibits a complex three-dimensional structure. For example, there is evidence of strong horizontal vortices near the interface of the rearward- and forward-relative flows above and below, respectively, the frontal boundary aloft (e.g. Figure 15a,b), which resemble the Kelvin–Helmholtz billows reported in laboratory and modelling studies of density currents. Similar structures were reported by Wakimoto and Bosart (2000) in high-resolution Doppler radar observations of an NCFR (see their figure 17e), suggesting that these model features are at least plausibly realistic. Additional vertical sections (not shown) reveal that the horizontal vortices are horizontally contiguous; the rearward vortex (labelled "VH2" in Figure 15b) is apparently associated with a secondary horizontal wind shift at the
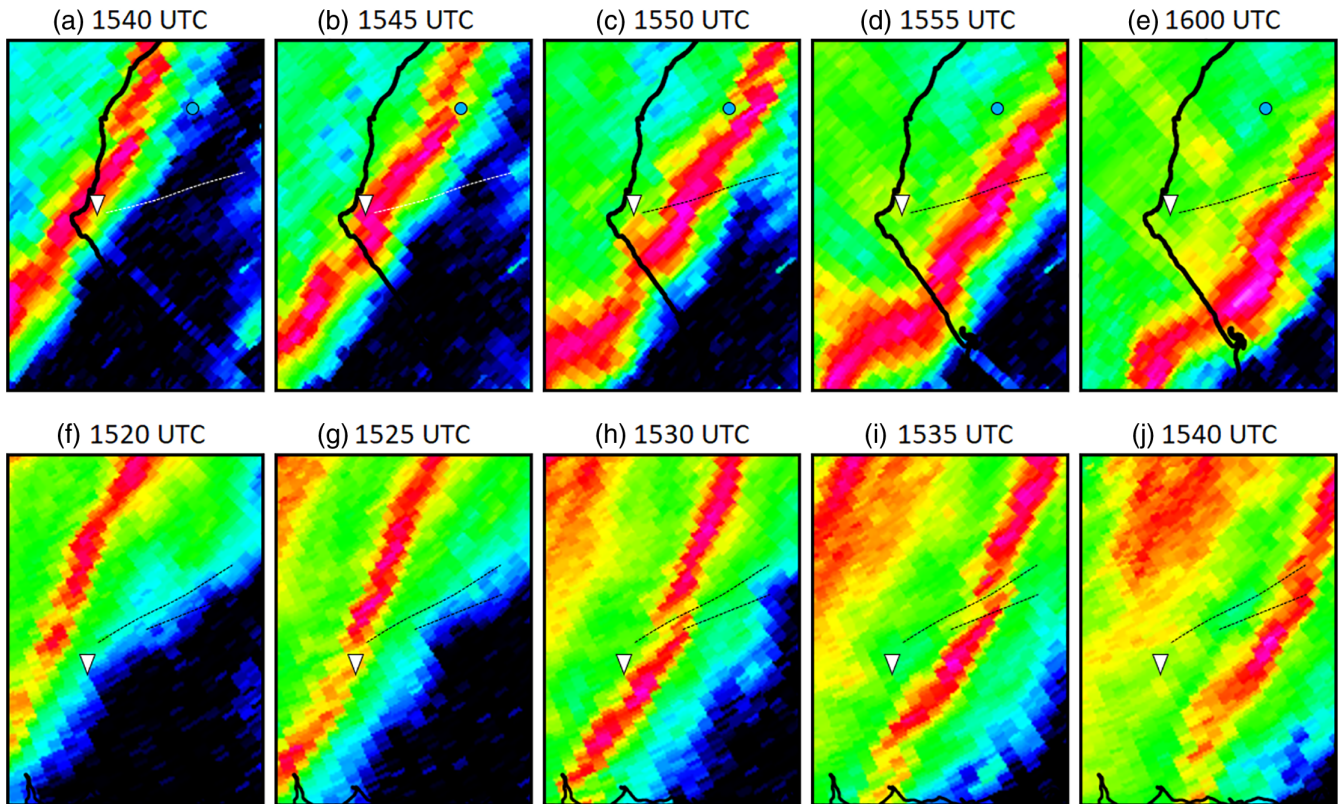
FIGURE 17 Sequence of 0.5° elevation angle radar reflectivity (colour scale as in Figure 16b) near to the two confirmed tornado reports (white inverted triangle in each panel). (a–e) Data from Hameldon Hill radar showing evolution of the NCFR near the Whitehaven, Cumbria, tornado. Location of an additional, non-tornadic, wind damage report is shown by the blue circle. (f–j) Data from Holehead radar showing evolution of the NCFR near to the Templand, Dumfries and Galloway, tornado. Area shown has width 62.5 km in all panels. Thin, dashed lines denote the tracks of NCFR gaps and inflections that pass close to the tornado reports. Coastlines are shown in black. Radar scan times are given above each panel [Colour figure can be viewed at wileyonlinelibrary.com]

surface, on the immediate cold side of the front (i.e. a secondary horizontal shear zone; examples are marked by the dashed red lines in various panels of Figure 13) and a prominent local MSLP minimum (marked by the dashed black line in Figure 13c, left panel). Beneath this horizontal vortex, the forward-directed, front-relative flow is locally enhanced and the theta contours bunch together strongly and descend closer to the surface (indicating a shallower cold pool capped by a layer of very strong static stability; Figure 15a,b). Between the main and secondary shear zones, the cold pool is locally deeper than elsewhere in the vertical sections, and the NCFR-relative winds are light.

6.4 | Comparison with radar observations

In order to aid operational recognition of miso-scale features potentially associated with NCFR tornadoes, and to support the suggestion that tornadoes in the real NCFR

were associated with miso-scale vortices similar to the secondary vortices in the 300 m simulation, we now present a comparison of the modelled and observed structure of the NCFR over part of the region exhibiting the strongest secondary vortices in the 300 m simulation (Figure 16). The model and observations agree closely in several respects. Firstly, relatively large perturbations are evident at intervals of approximately 50–70 km in the along-front direction which, in the model, can be seen to be associated with the remnants of primary vortices, or regions where vortices have amalgamated and grown up-scale whilst weakening (the tracks of these perturbations are indicated by bold dashed lines in Figure 16, and labelled V_{P1} and V_{P2} in Figure 16b). The along-front spacing of the larger inflections appears to be similar in the radar data and the 300 m simulation (cf. Figure 16a,b).

Secondly, smaller-scale perturbations, of typical wavelength 5–10 km, are evident in the modelled and observed NCFR between the tracks of the larger inflections. In the model, these perturbations are associated with the secondary, miso-scale vortices. The presence of vortices

of equivalent size in the real NCFR cannot be confirmed, owing to a lack of Doppler radar observations over northern England at the time of the event. However, the radar reflectivity field (Figure 16b) exhibits similar small-scale perturbations, comprising line bulges and occasional hooks and small NCFR breaks, superimposed on the larger-wavelength pattern described above. These features are suggestive of the presence of secondary vortices in the real NCFR.

Closer analysis of reflectivity data from the Hameldon Hill radar near to the Whitehaven tornado report (Figure 17a–e) shows that the tornado occurred at the up-front flank of a developing miso-scale NCFR inflection, as shown by the tornado report's positioning just to the northwest of the track of the centre of the inflection. The inflection only becomes apparent in the 1545 UTC scan (Figure 17b), suggesting that the associated miso-scale vortex was at an early stage in its development when the tornado occurred. A subtle reflectivity minimum develops near the inflection centre by 1600 UTC, resulting in the "broken-S" signature (Figure 17e). This signature becomes indistinct after 1600 UTC, suggesting that the tornado parent vortex was relatively short-lived.

A similar analysis for the Templand and Killowen tornadoes, using data from the nearest radars, also shows an association with developing miso-scale perturbations in the NCFR. For the Templand tornado, detailed analysis is precluded by the large range from radar, but the report is again situated close to a developing inflection and small NCFR break (Figure 17f–j). The (unconfirmed) Killowen tornado occurred near the centre of a shallow NCFR inflection, located immediately up-front of an intensifying reflectivity maximum (not shown). Therefore, all three tornadoes appear to have been associated with amplifying miso-scale NCFR perturbations resembling those associated with secondary vortices in the 300 m simulation.

7 | DISCUSSION

In the preceding sections we have explored how a developing frontal wave influences the timing and location of meso-γ- to miso-scale vortex-genesis along a vertical vortex sheet coincident with an NCFR, and we have described the structure and evolution of selected vortices. In this section we further consider the possible vortex-genesis mechanisms and compare our results with those of previous studies of meso-γ- to miso-scale vortices within NCFRs and quasi-linear convective systems (QLCSs) more generally.

Considering the various possible vortex-genesis mechanisms, we suggest HSI to be the most likely, as supported by the following evidence:

1. Primary vortices exhibited fairly regular along-front spacing, and vortices were like-signed (i.e. all cyclonic); no evidence of cyclonic–anticyclonic vortex pairs was found (such vortex pairs would be expected in the early stages of development if tilting of horizontal vorticity were the relevant vortex-genesis mechanism: for example, Weisman and Davis, 1998; Trapp and Weisman, 2003; Atkins and St. Laurent, 2009).

2. The spacing of primary vortices in the 1.5 km and 300 m simulations conforms closely to that predicted by linear theory for the most unstable mode (i.e. $7.5 \times$ initial shear zone width: Miles and Howard, 1964). Details of the vortex-spacing calculations are presented in Appendix B.

3. The associated pattern of roughly ovoid vortex cores (when viewed in horizontal section), separated by narrowing braids along which the horizontal convergence was maximised, and the breaking wave structure in low-level temperature and vorticity fields (e.g. Figure 11), strongly resemble the structures reported in idealised simulations of HSI (e.g. figure 7 of Buban and Zeigler, 2016).

4. In the pseudo-Lagrangian reference frame of individual vortices, primary vortex-genesis occurred close to the time of transition from positive to negative S_{HSI}. This is consistent with the release of HSI, in a situation where the release was formerly supressed by the large cross-frontal confluence, following the results of Dritschel *et al.* (1991).

A caveat to the final point is that the magnitude and sign of S_{HSI} has a strong height dependency, as revealed by calculation of values on different model levels between the surface and 3.5 km AGL (not shown). In general, S_{HSI} increases with decreasing height within the boundary layer due to surface friction (which acts to increase the horizontal convergence, relative to the vertical vorticity, along the shear zone). Down-front of the wave centre, in the region of $S_{HSI} < 0$ at 1,390 m AGL, the height of transition to positive values is low compared to the mean depth of the shear zone; in other words, most of the shear zone experiences $S_{HSI} < 0$. In contrast, elsewhere along the front, the shear zone is shallower whilst the height of transition is greater, or S_{HSI} is positive at all heights, such that most or all of the shear zone is situated within $S_{HSI} > 0$. We are not aware of any studies pertaining to the stability of vortex strips in vertically varying stretching deformation fields, but it may be speculated that the release of HSI is more likely where the height of transition to $S_{HSI} < 0$ is low, relative to the depth of the shear zone, as is the case immediately down-front of the wave centre. These aspects are explored further in Appendix C.

In the current case, the radar-observed development of miso-scale NCFR perturbations including inflections, broken-S signatures and occasional hooks akin to those in the 300 m model strongly suggests that miso-scale vortices were present in the real NCFR (cf. Figure 16a,b) although, in the absence of Doppler radar observations, this cannot be confirmed. The association between miso-scale vortices, NCFR perturbations and tornadoes has been demonstrated in previous studies of tornadic NCFRs where Doppler radar data were available (e.g. Carbone, 1983; Clark and Parker, 2014), and is suggested in the current study by the proximity of tornado reports to developing NCFR perturbations. Whilst existing studies appear consistent in this respect, analysis of Doppler radar observations for a larger set of NCFR tornadoes would be beneficial for furthering our understanding of the association between tornadoes and miso-scale vortices, and of the positioning of tornadoes relative to the associated vortices and NCFR perturbations, more generally.

The observed sub-structure of the secondary vortices in the 300 m simulations agrees closely with that reported in previous simulations of miso-scale NCFR vortices. For example, in a real data simulation of the 24 September 2007 NCFR, Smart and Browning (2009) found a vertical vorticity stretching maximum at the northern flank of their modelled vortices, which they likewise suggested to be a potential location for tornadogenesis. Other similarities (cf. their figure 7) include the relative shallowness of vortices (typical depth $\sim$ 2–3 km), the occurrence of the largest vertical vorticity at low levels (<0.5 km AGL), the presence of a downdraught wrapping around the down-front flank of the vortex at low levels, the core of strong winds (>25 m·s^{-1}) on the down-front flank of the vortex, and the association of vortices with localised NCFR perturbations including inflections and broken-S-type structures. Apsley *et al.* (2016) similarly noted wind maxima on the equatorward flank of their simulated miso-scale vortices, in a reanalysis of the cold-frontal tornado outbreak of 23 November 1981. However, unlike in the present case, Apsley *et al.* (2016) reported the frequent occurrence of cyclonic–anticyclonic vortex pairs. This difference suggests that the vortex-genesis mechanisms may vary from case to case.

The development of >25 m·s^{-1} wind cores on the equatorward flanks of simulated miso-scale vortices provides a possible explanation for reports of localised non-tornadic wind damage in NCFRs, as previously suggested by Smart and Browning (2009). An example is shown in Figure 17a–e; the blue dot marks the location of localised non-tornadic wind damage, which occurred near the centre of a small NCFR bulge on the southern flank of a small broken-S signature. However, with typical diameters of 1–3 km, we suggest these cores are unlikely

to explain the majority of NCFR tornado reports, since damage site investigations show the tornadoes to have typical track widths of around 50–100 m.[11] As noted by Smart and Browning (2009), the potential for both tornadic and non-tornadic wind damage in association with miso-scale vortices does highlight a need for careful investigation of individual NCFR damage reports, in order to ensure the proper classification of damage as tornadic or otherwise.

The similarity in the structure of the primary and secondary vortices in the 300 m simulation, and of the wind, temperature and pressure fields in their vicinity (e.g. cf. Figures 11d and 13g), is striking. This similarity suggests that the sequential evolution of primary vortices, followed by smaller-scale secondaries along the braids between them, may be an example of the self-similar cascade of filament instabilities described by Scott and Dritschel (2014), wherein vortex sheet roll-up repeatedly occurs along the braids between existing vortices, down to very small scales. If so, a natural question arising is whether tertiary (and further) vortex-genesis might be simulated along the braids between the secondary vortices, given a model with sufficiently small grid spacing. This scenario raises the possibility that tornado-like vortices in NCFRs result from the development of braid instabilities at scales unresolved in the simulations presented here (rather than within the region of intense near-surface vertical vorticity stretching on the flanks of the secondary vortices, as previously suggested). Higher-resolution simulations (ideally, with grid spacing <100 m) would be required to investigate these possibilities.

A noticeable characteristic of the larger NCFR perturbations (i.e. broken-S signatures and the residual NCFR gaps) in both the 1.5 km and 300 m simulations was their longevity. The NCFR gaps often far outlived the vortices originally responsible for their development and they were associated with local minima in cross-frontal wind and temperature gradients, as found in previous observational studies (e.g. James and Browning, 1979). This longevity, coupled with down-front movement relative to the wave centre, meant that NCFR gaps eventually migrated towards the trailing part of the front several hundred kilometres down-front of the wave centre. The persistence of the NCFR gaps and the clockwise-turned NCFR cores between them may help to explain why

---

[11]Of the tornadoes associated with the set of 44 tornadic cold fronts analysed by CP20, maximum track width estimates are available in the TORRO tornado database for 51, where track width is recorded using an 11-point scale (see table 1 of Kirk, 2007). The median and modal track width category of these tornadoes is W5 (maximum track width in the range 47–99 m). The minimum track width category (one tornado) was W1 (2.2–4.6 m) and the maximum track width category (3 tornadoes) was W7 (maximum track width in the range 216–414 m).

this kind of core–gap morphology has been so widely reported in previous studies of NCFRs (e.g. Hobbs and Biswas, 1979; James and Browning, 1979; Hobbs and Persson, 1982; Browning and Roberts, 1996; Jorgensen *et al.*, 2003; Kawashima, 2007). Whilst it has sometimes been suggested that NCFR gaps represent preferred locations for tornadoes, our results suggest a distinction should be made between the smaller, amplifying perturbations associated with rapidly developing vortices (especially the miso-scale secondary vortices) and the larger, slowly evolving, step-like features and NCFR gaps associated with decaying or decayed vortices; tornadoes appear possible with the former, but highly unlikely with the latter.

Previous studies show that NCFR tornadoes are more likely where convective available potential energy (CAPE) is non-zero (e.g. Clark, 2013; Apsley *et al.*, 2016), or where moist static instability exists in the pre-frontal environment (Clark and Parker, 2014). In the present case, the immediate pre-frontal environment near the wave centre was sampled by the 1200 UTC 17 October Castor Bay (Northern Ireland) sounding. Modification with 1200 UTC surface observations from various sites shows generally meagre CAPE ($<\sim50$ J·kg^{-1}) at inland locations, but rather larger CAPE (typically 50–200 J·kg^{-1}) close to windward coasts (with respect to the south–southwesterly pre-frontal wind direction). It is noticeable that the two confirmed tornadoes occurred within ~20 km of a windward coast (e.g. Figure 12). In light of these results we suggest that, whilst the frontal wave provides the requisite conditions for vortex-genesis along the shear zone, and determines the region at risk of tornadoes on the mesoscale, horizontal variability in pre-frontal CAPE may also act to modulate the tornado risk on smaller scales. The discussion of buoyant instability and its spatial variability is also relevant given the results of Moore (1985), who demonstrated the existence of a hybrid buoyancy–shearing instability in NCFRs under certain combinations of horizontal shear and static stability. Further research in this area would be beneficial to determine, for example, whether transitions can occur between pure shearing instability and the buoyancy–shear hybrid mode in an individual NCFR, and if so, how such transitions might impact on the structure and intensity of vortices and the associated tornado risk.

8 | CONCEPTUAL FRAMEWORK

In this section we provide a synthesis of the results in the form of a conceptual model (Figure 18). Although this conceptual model is based largely on the findings of the current study, we are confident that it has some wider

applicability. This is partly because the event was selected on the basis that it was a good example of the type of frontal wave found by CP20 to be associated with a majority of tornadic NCFRs, but also because many of the characteristic features were evident in similar (though less detailed) analyses of other frontal wave cases using 1.5 km model simulations, the results of which are not presented in the current article.

Considering first the synoptic scale (Figure 18a), the initial condition is a trailing cold front, located underneath the forward flank of a broad upper-level trough and orientated at a shallow angle ($<45°$) to the upper-level flow, and in which the low-level flow pattern is at least weakly frontogenetic. The latter condition is necessary because the evolution described requires a well-defined surface cold front and associated narrow zone of horizontal wind shear (i.e. a vertical vorticity strip) at the outset of frontal wave development; in other words, the narrow shear zone is "pre-existing" in the context of the frontal wave development (or, at the least, minimal cross-frontal contraction is required to realise a narrow shear zone).[12]

An upper-level jet streak and associated positive PV anomaly move around the axis of the long-wave upper-level trough; as these features approach the trailing cold front, secondary cyclogenesis commences (Figure 18b–d). The associated frontal wave sets up mesoscale spatio-temporal variations in vertical vorticity and horizontal confluence that favour meso-γ- to miso-scale vortex-genesis along the shear zone near and just down-front of the wave centre as the wave amplifies (as signified by the pink and red dots along the front in Figure 18b–d), where the front begins to rotate cyclonically. In detail, the evolution in this region begins with increasing frontogenesis, cross-frontal confluence and vertical vorticity at the outset of wave development. With continued development, frontogenesis and cross-frontal confluence begin to decrease, whilst the vorticity continues to increase. Vortex-genesis by horizontal shearing instability occurs due to the contemporaneous increases in vertical vorticity and decreases in the cross-frontal confluence at this stage of wave development, which

---

[12]Operational experience provides many examples of frontal waves (and indeed primary cyclones) in which a narrow frontal shear zone and associated NCFR fail to develop. In other cases, they may develop only along the trailing part of the cold front, well down-front of the wave centre, or at the developing bent-back front (e.g. Browning and Roberts, 1994; 1996), and therefore not in the otherwise tornado-favourable region. The lack of an NCFR immediately down-front of the wave centre in the early developmental stages therefore appears to constitute an important tornadogenesis failure mode. Analysis of the total frontogenesis within this part of the cyclone may be useful in this regard, as a measure of NCFR probability (as discussed in Appendix A of CP20).
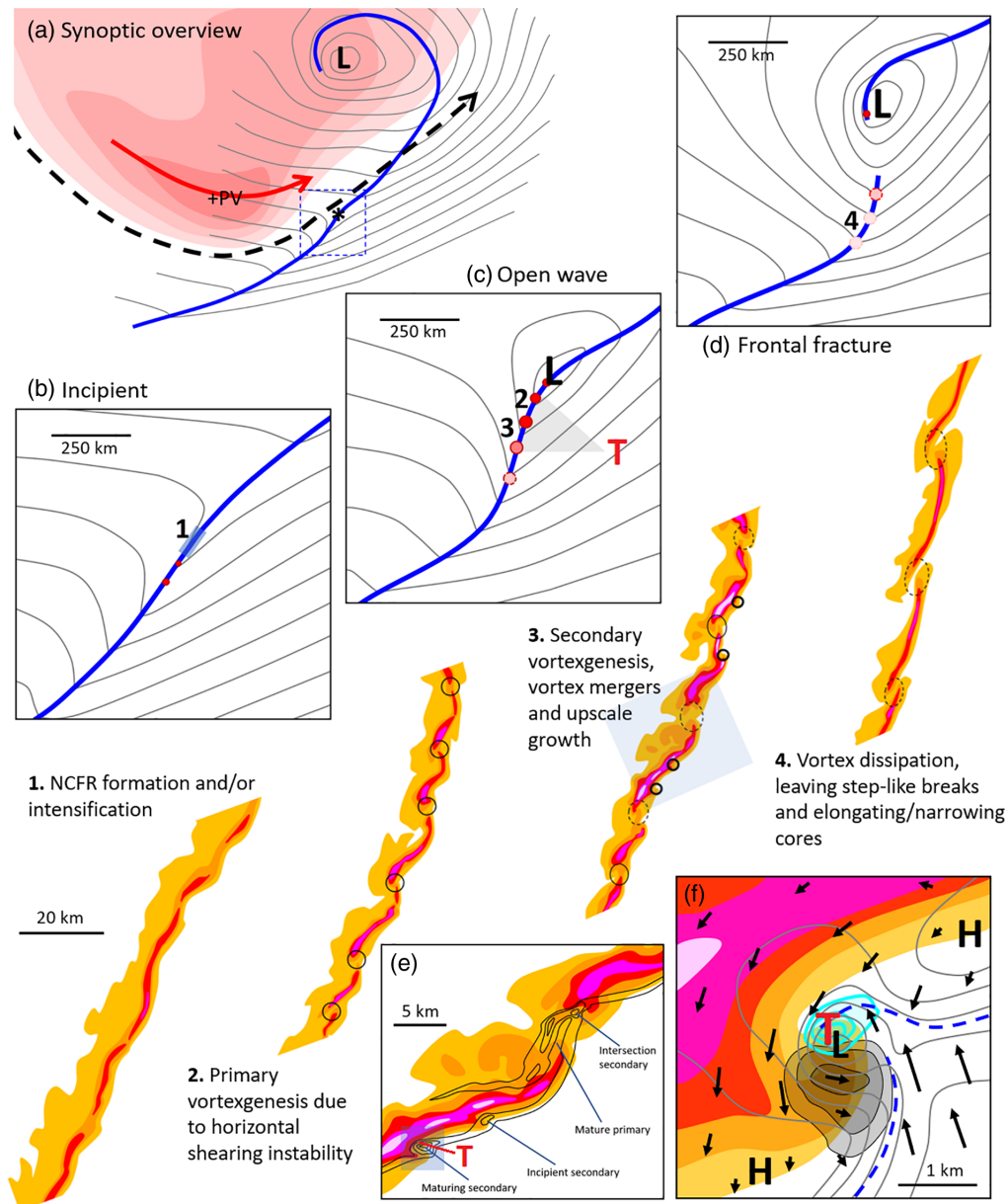
FIGURE 18 Conceptual model depicting the typical development in a tornadic frontal wave from the synoptic-scale (top, left) to the miso-scale (bottom, right). (a) Synoptic-scale overview at the incipient stage of frontal wave development. Red shading denotes region of large PV at 300 hPa (darker shading for larger values); red arrow denotes the front-relative movement of the PV maximum (+PV). Dashed arrow marks the approximate position of the upper-level jet axis. Grey contours are MSLP at ~4 hPa intervals. Bold blue line indicates the position of the surface front. Dashed blue box indicates the domain shown in (b). "L" denotes the parent low-pressure centre and the asterisk the frontal wave centre. (b–d) Evolution of the developing frontal wave on the meso-α-scale, showing three stages: (b) incipient; (c) open wave; and (d) frontal fracture. MSLP (grey contours) is plotted at ~2 hPa intervals. Bold blue line indicates position of surface front. "L" indicates the centre of the frontal wave. Red/pink circles denote meso-γ- to miso-scale vortex-genesis (along-front spacing of individual vortices not to scale; deeper red shades indicate developing vortices and pink indicates decaying vortices or residual step-like NCFR breaks). In (c), the section of front prone to tornadoes is indicated by the grey shading and letter "T". Main panel: four stages of NCFR development, (1)–(4), as described by the annotations in the figure. Shading depicts near-surface rainfall rate (pink > magenta > red > orange > yellow). Blue shaded box at stage (3) depicts the region shown in (e). Black circles indicate locations of vortices (dashed where vortices are weakening, and bold for secondary vortices). (e) Zoomed-in view of part of the NCFR during stage (3), showing the typical location of secondary vortices relative to the larger NCFR perturbations associated with a decaying primary vortex (see annotations in the panel for details). Blue shaded box depicts the region shown in (f). "T" indicates the most likely location for a tornado. Black contours denote near-surface vertical vorticity. (f) Zoomed-in view of one of the secondary vortices near the time of peak intensity. Cyan contours depict the vertical vorticity stretching maximum, and grey contours the core of strong (>~25 m·s⁻¹) winds. Arrows depict vortex-relative wind vectors near ground level. Yellow-red-pink shading denotes rainfall rate, and grey contours depict MSLP at ~0.5 hPa intervals. Dashed blue lines show the leading edge of the primary shear zone. "T" indicates the most likely location for a tornado [Colour figure can be viewed at wileyonlinelibrary.com]

allows release of HSI in a situation where the release was formerly suppressed by the large cross-frontal confluence (consistent with previous theoretical work on the stability of vortex strips in the presence of horizontal stretching deformation fields: e.g. Dritschel *et al.*, 1991).

Frontolysis and cross-frontal diffluence eventually evolve in the vortex-prone region, resulting in frontal fracture and dissipation of the NCFR here (Figure 18d). Conversely, the NCFR tends to persist for longer along the trailing part of the front far down-front of the wave centre. This evolution means that vortex-genesis (and associated tornado risk) is generally restricted to the early developmental stages of the secondary cyclone's life cycle.[13] In the analysed case, individual vortices moved down-front relative to the frontal wave; however, we suggest that the wave-relative movement of individual vortices may vary from case to case.

On the meso-β- to meso-γ-scales, vortex-genesis results in the transition of an initially fairly two-dimensional, unbroken NCFR (stage 1 in Figure 18) to one exhibiting marked core–gap structure near to, and just down-front of, the wave centre (stage 2). In practice, intensification of the NCFR may occur in tandem with the onset of secondary cyclogenesis (due to the increasing frontogenesis at this stage). The period with a relatively linear, unbroken NCFR may therefore be short-lived, and we suggest that it may not always be evident in radar data (especially where the wave moves rapidly and where the onset of wave development occurs at large range from the nearest radars). Notwithstanding this issue, the presence of amplifying perturbations within an NCFR, including newly developing NCFR gaps and associated broken-S reflectivity structures (McAvoy *et al.*, 2000; Grumm and Glazewski, 2004; Lane and Moore, 2006), may be taken as an indication of the presence of developing vortices, with associated risk of tornadoes and localised non-tornadic wind damage.

On the other hand, residual inflections and gaps may persist in the NCFR for a period of several hours following individual vortex merger and decay, resulting in a persistent core–gap structure in the trailing NCFR well down-front of the wave centre (stage 4). These residual inflections and gaps tend to evolve slowly and are associated with local minima in the cross-frontal temperature and wind gradients. For this reason, they are unlikely to be favoured locations for tornadoes or localised

---

[13]A few cases are known, however, in which vortex-genesis and tornadoes occurred after frontal fracture, near the tip of the developing bent-back front (at the location denoted by the northern red dot in Figure 18d). Such development appears atypical, and the few cases analysed to date all involved unusually small frontal waves with wavelengths on the order of tens of kilometres (e.g. Clark, 2013; Young and Clark, 2018).

non-tornadic wind damage, and as such a distinction should be made between these residual perturbations and the rapidly evolving perturbations associated with developing vortices.

The largest values of near-surface vertical vorticity and vertical vorticity stretching, and we suggest the greatest potential for tornadoes, occur in association with miso-scale secondary vortices that develop and intensify extremely rapidly along the braid regions between existing primary vortices (stage 3; Figure 18e). These secondary vortices therefore occur along the intense precipitation cores between the larger NCFR gaps or inflections associated with the primary vortices. Perturbations in the NCFR cores associated with the secondary vortices are small and may not be evident until after the time of tornadogenesis, but they include small hook or appendage echoes near the southern flank of vortices, and inflow notches on the northern flank (Figure 18e–f). Tornadogenesis appears most likely within a small zone of intense near-surface vertical vorticity stretching on the north, northwest, or west flanks of the secondary vortices (Figure 18f). This flanking stretching maximum is typically strongest during the developing and early-mature stages of secondary vortex evolution. Larger, though still highly localised, cores of strong winds (up to 25–35 m·s^{-1}, with typical diameters of 1–3 km) develop along the down-front flanks of the same vortices during their mature to early dissipating stages of evolution, during which period the vortices often expand steadily whilst weakening. These wind maxima are a potential source of localised non-tornadic wind damage in NCFRs.

9 | CONCLUSIONS

In this article we have used observations and model output to investigate the structure and evolution of a tornadic NCFR within a frontal wave. The selected case is part of a significant class of tornadic NCFRs identified by CP20, suggesting that the results have some wider relevance. The results may be summarised as follows:

1. Secondary cyclogenesis (on the meso-α-scale) strongly modulates the risk of tornadoes along the NCFR
2. As the wave develops, numerous primary (meso-γ-scale) and secondary (miso-scale) vortices develop along a narrow zone of strong vertical vorticity coincident with the surface front and NCFR, just down-front of the wave centre.
3. Circumstantial evidence has been presented that HSI is the responsible mechanism for vortex-genesis on the meso-γ- and miso-scales. We suggest that the release of HSI is initially supressed by the substantial

cross-frontal confluence at the trailing front (which is also instrumental in promoting development and/or maintenance of a narrow frontal shear zone in the first place); however, as wave development ensues, simultaneous increases in vertical vorticity and decreases in cross-frontal confluence allow for release of HSI in a well-defined region down-front of the wave centre. Vortex-genesis ceases with transition to cross-frontal diffluence and associated frontal fracture.

4. In the high-resolution simulations, the strongest near-surface vertical vorticity maxima and highest wind speeds were associated with miso-scale secondary vortices (typical diameters 1–3 km) that developed extremely rapidly at the leading edge of precipitation cores along the braid regions between larger perturbations associated with mature or decaying primary vortices.

5. These secondary vortices likely constitute preferred locations for tornadogenesis, as supported by analysis of radar data near to the two confirmed tornadoes in the real NCFR.

We suggest that the results presented herein, together with those of CP20, provide a provisional framework for the improved operational recognition of tornado-favourable environments in frontal waves, a situation that accounts for the majority of tornadic NCFRs (55%) and NCFR tornado outbreaks (73% of events producing ≥7 tornadoes) in the United Kingdom and Ireland. Whilst we are confident that the synoptic- to meso-scale evolution has some generality, the detailed sequence of meso-γ-scale primary vortex-genesis followed by miso-scale secondary vortex-genesis may be more case-dependent. Similar studies of other frontal wave NCFRs would therefore be desirable to assess the generality (or otherwise) of this behaviour. Remaining gaps in understanding include the possible variability in vortex-genesis mechanisms from case to case, the details of tornadogenesis within the miso-scale vortices, and the relevance of buoyant instability to the tornadogenesis process. Finally, although we have provided evidence that the miso-scale structures were captured credibly by the 300 m model, the miso-scale is only marginally resolved here (as discussed in Appendix B). For this reason, it would be desirable to nest to even higher resolution (grid spacing ≤100 m) in future simulations of tornadic NCFRs. Such simulations would permit a deeper exploration of the rich three-dimensional structure of the secondary vortices and of the frontal shear zone along which they form.

ACKNOWLEDGEMENTS

AUTHOR CONTRIBUTIONS

Matthew Clark: Formal analysis; investigation; methodology; software; visualization; writing – original draft; writing – review and editing. **Douglas Parker:** Supervision; writing – original draft; writing – review and editing. **Kirsty Hanley:** Data curation; software.

ORCID

M. R. Clark https://orcid.org/0000-0002-0982-9363
D. J. Parker https://orcid.org/0000-0003-2335-8198
K. E. Hanley https://orcid.org/0000-0002-1002-7667

REFERENCES

Adlerman, E.J. and Droegemeier, K.K. (2005) The dependence of numerically simulated cyclic mesocyclogenesis upon environmental vertical wind shear. *Monthly Weather Review*, 133, 3595–3623.

Apsley, M., Mulder, K.J. and Schultz, D.M. (2016) Reexamining the United Kingdom's greatest tornado outbreak: forecasting the limited extent of tornadoes along a cold front. *Weather and Forecasting*, 31, 853–875.

Atkins, N.T. and St. Laurent, M. (2009) Bow echo mesovortices. Part II: Their genesis. *Monthly Weather Review*, 137, 1514–1532.

Bishop, C.H. and Thorpe, A.J. (1994) Frontal wave stability during moist deformation frontogenesis. Part II: The suppression of nonlinear wave development. *Journal of the Atmospheric Sciences*, 51, 874–888.

Brown, P.R. and Meaden, G.T. (2012) TORRO tornado division report: September–October 2011. *International Journal of Meteorology*, 37, 27–30.

Browning, K.A. and Golding, B.W. (1995) Mesoscale aspects of a dry intrusion within a vigorous cyclone. *Quarterly Journal of the Royal Meteorological Society*, 121(523), 463–493.

Browning, K.A. and Reynolds, R. (1994) Diagnostic study of a narrow cold-frontal rainband and severe winds associated with a stratospheric intrusion. *Quarterly Journal of the Royal Meteorological Society*, 120(516), 235–257.

Browning, K.A. and Roberts, N.M. (1994) Structure of a frontal cyclone. *Quarterly Journal of the Royal Meteorological Society*, 120(520), 1535–1557.

Browning, K.A. and Roberts, N.M. (1996) Variation of frontal and precipitation structure along a cold front. *Quarterly Journal of the Royal Meteorological Society*, 122(536), 1845–1872.

Buban, M.S. and Zeigler, C.L. (2016) The formation of small-scale atmospheric vortices via horizontal shearing instability. *Journal of the Atmospheric Sciences*, 73, 2061–2084.

Carbone, R.E. (1982) A severe frontal rainband. Part I. Stormwide hydrodynamic structure. *Journal of the Atmospheric Sciences*, 39, 258–279.

Carbone, R.E. (1983) A severe frontal rainband. Part II. Tornado parent vortex circulation. *Journal of the Atmospheric Sciences*, 40, 2639–2654.

Clark, M.R. (2013) A provisional climatology of cool-season convective lines in the UK. *Atmospheric Research*, 123, 180–196.

Clark, M.R. and Parker, D.J. (2014) On the mesoscale structure of surface wind and pressure fields near tornadic and nontornadic cold fronts. *Monthly Weather Review*, 142, 3560–3585.

Clark, M.R. and Parker, D.J. (2020) Synoptic-scale and mesoscale controls for tornadogenesis on cold fronts: a generalised measure of tornado risk and identification of synoptic types. *Quarterly Journal of the Royal Meteorological Society*, 146(733), 4195–4225.

Clark, M. and Smart, D. (2016) Supercell and non-supercell tornadoes in the United Kingdom and Ireland. In Doe, R.K. (Ed.) *Extreme Weather. Forty Years of the Tornado and Storm Research Organisation (TORRO)*. Chichester, UK: Wiley Blackwell, pp. 31–59.

Dahl, J.M.L. (2020) Near-surface vortex formation in supercells from the perspective of vortex patch dynamics. *Monthly Weather Review*, 148, 3533–3547.

Davies, T., Cullen, M.J.P., Malcolm, A.J., Mawson, M.H., Staniforth, A., White, A.A. and Wood, N. (2005) A new dynamical core for the Met Office's global and regional modelling of the atmosphere. *Quarterly Journal of the Royal Meteorological Society*, 131(608), 1759–1782.

Dee, D.P., Uppala, S.M., Simmons, A.J., Berrisford, P., Poli, P., Kobayashi, S., Andrae, U., Balmaseda, M.A., Balsamo, G., Bauer, P., Bechtold, P., Beljaars, A.C.M., van de Berg, L., Bidlot, J., Bormann, N., Delsol, C., Dragani, R., Fuentes, M., Geer, A.J., Haimberger, L., Healy, S.B., Hersbach, H., Hólm, E.V., Isaksen, L., Kållberg, P., Köhler, M., Matricardi, M., McNally, A.P., Monge-Sanz, B.M., Morcrette, J.J., Park, B.K., Peubey, C., de Rosnay, P., Tavolato, C., Thépaut, J.N. and Vitart, F. (2011) The ERA-Interim reanalysis: configuration and performance of the data assimilation system. *Quarterly Journal of the Royal Meteorological Society*, 137(656), 553–597.

Dritschel, D.G., Haynes, P.H., Juckes, M.N. and Shepherd, T.G. (1991) The stability of a two-dimensional vorticity filament under uniform strain. *Journal of Fluid Mechanics*, 230, 647–665.

Fujita, T.T. (1981) Tornadoes and downbursts in the context of generalized planetary scales. *Journal of the Atmospheric Sciences*, 38, 1511–1534.

Grumm, R.H. and Glazewski, M. (2004) Thunderstorm types associated with the 'broken-S' radar signature. *Preprints*, *22nd Conference on Severe Local Storms*, *4–8 October 2004*, *Myannis*, *MA*. Boston, MA: American Meteorological Society. CD-ROM: P7.1.

Hanley, K.E., Barrett, A.I. and Lean, H.W. (2016) Simulating the 20 May 2013 Moore, Oklahoma tornado with a 100-metre grid-length NWP model. *Atmospheric Science Letters*, 17, 453–461.

Hanley, K.E., Plant, R.S., Stein, T.H.M., Hogan, R.J., Nicol, J.C., Lean, H.W., Halliwell, C. and Clark, P.A. (2015) Mixing-length controls on high-resolution simulations of convective storms. *Quarterly Journal of the Royal Meteorological Society*, 141(686), 272–284.

Harrold, T.W. (1973) Mechanisms influencing the distribution of precipitation within baroclinic disturbances. *Quarterly Journal of the Royal Meteorological Society*, 99(420), 232–251.

Harvey, B., Methven, J., Eagle, C. and Lean, H. (2017) Does the representation of flow structure and turbulence at a cold front converge on multiscale observations with model resolution? *Monthly Weather Review*, 145, 4345–4363.

Hastie, T., Tibshirani, R. and Friedman, J. (2009) *The Elements of Statistical Learning. Data Mining, Inference, and Prediction*, 2nd edition. New York, NY: Springer-Verlag.

Hobbs, P.V. and Biswas, K.R. (1979) The cellular structure of narrow cold-frontal rainbands. *Quarterly Journal of the Royal Meteorological Society*, 105(445), 723–727.

Hobbs, P.V. and Persson, P. (1982) The mesoscale and microscale structure and organization of clouds and precipitation in midlatitude cyclones. Part V: The substructure of narrow cold-frontal rainbands. *Journal of the Atmospheric Sciences*, 39, 280–295.

Hoskins, B.J. and Bretherton, F.P. (1972) Atmospheric frontogenesis models: mathematical formulation and solution. *Journal of the Atmospheric Sciences*, 29, 11–37.

Houze, R.A.Jr., Hobbs, P.J., Biswas, K.R. and Davis, W.M. (1976) Mesoscale rainbands in extratropical cyclones. *Monthly Weather Review*, 104, 868–878.

James, P.K. and Browning, K.A. (1979) Mesoscale structure of line convection at surface cold fronts. *Quarterly Journal of the Royal Meteorological Society*, 105(444), 371–382.

Jorgensen, D.P., Pu, Z., Persson, P. and Tao, W.-K. (2003) Variations associated with cores and gaps of a Pacific narrow cold frontal rainband. *Monthly Weather Review*, 131, 2705–2729.

Kawashima, M. (2007) Numerical study of precipitation core–gap structure along cold fronts. *Journal of the Atmospheric Sciences*, 64, 2355–2377.

Kirk, P. (2007) UK tornado climatology, 1980–2004. *International Journal of Meteorology*, 32, 158–172.

Kundu, P.K. and Cohen, I.M. (2004) *Fluid Mechanics*, 3rd edition. Salt Lake City, UT: Academic Press.

Lane, J.D. and Moore, P.D. (2006) Observations of a non-supercell tornadic thunderstorm from terminal Doppler weather radar. *Preprints*, *23rd Conference Severe Local Storms*, *St. Louis*, *MO*. Boston, MA: American Meteorological Society. CD-ROM: P4.5.

Lean, H.W. and Clark, P.A. (2003) The effects of changing resolution on mesoscale modelling of line convection and slantwise circulations in FASTEX IOP16. *Quarterly Journal of the Royal Meteorological Society*, 129(592), 2255–2278.

Lee, B.D. and Wilhelmson, R.B. (1997) The numerical simulation of non-supercell tornadogenesis. Part I: Initiation and evolution of pretornadic misocyclone circulations along a dry outflow boundary. *Journal of the Atmospheric Sciences*, 54, 32–60.

Matejka, T.J., Houze, R.A., Jr. and Hobbs, P.V. (1980) Microphysics and dynamics of clouds associated with mesoscale rainbands in extratropical cyclones. *Quarterly Journal of the Royal Meteorological Society*, 106(447), 29–56.

McAvoy, B.P., Jones, W.A. and Moore, P.D. (2000) Investigation of an unusual storm structure associated with weak to occasionally

strong tornadoes over the eastern United States. *Preprints, 20th Conference Severe Local Storms, Orlando, FL*. Boston, MA: American Meteorological Society, 182–185.

Miles, J.W. and Howard, L.N. (1964) Note on heterogeneous shear flow. *Journal of Fluid Mechanics*, 20, 331–336.

Moore, G.W.K. (1985) The organization of convection in narrow cold-frontal rainbands. *Journal of the Atmospheric Sciences*, 42, 1777–1791.

Mulder, K.J. and Schultz, D.M. (2015) Climatology, storm morphologies, and environments of tornadoes in the British Isles: 1980–2012. *Monthly Weather Review*, 143, 2224–2240.

Mulqueen, K.C. and Schultz, D.M. (2015) Non-classical extratropical cyclones on Met Office sea-level pressure charts: double cold and warm fronts. *Weather*, 70(3), 100–105.

Nicol, J.C., Hogan, R.J., Stein, T.H.M., Hanley, K.E., Clark, P.A., Halliwell, C.E., Lean, H.W. and Plant, R.S. (2015) Convective updraught evaluation in high-resolution NWP simulations using single-Doppler radar measurements. *Quarterly Journal of the Royal Meteorological Society*, 141(693), 3177–3189.

Okubo, A. (1970) Horizontal dispersion of floatable particles in the vicinity of velocity singularities such as convergences. *Deep Sea Research*, 17, 445–454.

Orlanski, I. (1975) A rational subdivision of scales for atmospheric processes. *Bulletin of the American Meteorological Society*, 56, 527–530.

Parsons, D.B. and Hobbs, P.V. (1983) The mesoscale and microscale structure and organization of clouds and precipitation in midlatitude cyclones. XI: Comparisons between observational and theoretical aspects of rainbands. *Journal of the Atmospheric Sciences*, 40, 2377–2397.

Reynolds, D.J. (1999) A revised UK tornado climatology, 1960–1989. *Journal of Meteorology (UK)*, 24, 290–321.

Scott, R.K. and Dritschel, D.G. (2014) Numerical simulation of a self-similar cascade of filament instabilities in the surface quasigeostrophic system. *Physical Review Letters*, 112, 144505.

Schielicke, L., Névir, P. and Ulbrich, U. (2016) Kinematic vorticity number – a tool for estimating vortex sizes and circulations. *Tellus A*, 68, 29464.

Shapiro, M.A. and Keyser, D. (1990) Fronts, jet streams and the tropopause. In Newton, C.W. and Holopainen, E.O. (Eds.) *Extratropical Cyclones, the Erik Palmen Memorial Volume*. Boston, MA: American Meteorological Society, pp. 167–191.

Smart, D.J. and Browning, K.A. (2009) Morphology and evolution of cold-frontal misocyclones. *Quarterly Journal of the Royal Meteorological Society*, 135(639), 381–393.

Trapp, R.J. and Weisman, M.L. (2003) Low-level mesovortices within squall lines and bow echoes. Part II: Their genesis and implications. *Monthly Weather Review*, 131, 2804–2823.

Wakimoto, R.M. and Bosart, B.L. (2000) Airborne radar observations of a cold front during FASTEX. *Monthly Weather Review*, 128, 2447–2470.

Walters, D., Boutle, I., Brooks, M., Melvin, T., Stratton, R., Vosper, S., Wells, H., Williams, K., Wood, N., Allen, T., Bushell, A., Copsey, D., Earnshaw, P., Edwards, J., Gross, M., Hardiman, S., Harris, C., Heming, J., Klingaman, N., Levine, R., Manners, J., Martin, G., Milton, S., Mittermaier, M., Morcrette, C., Riddick, T., Roberts, M., Sanchez, C., Selwood, P., Stirling, A., Smith, C., Suri, D., Tennant, W., Vidale, P.L., Wilkinson, J., Willett, M., Woolnough, S. and Xavier, P. (2017) The Met Office Unified Model global atmosphere 6.0/6.1 and JULES global land 6.0/6.1 configurations. *Geoscientific Model Development*, 10, 1487–1520.

Weisman, M.L. and Davis, C.A. (1998) Mechanisms for the generation of mesoscale vortices within quasi-linear convective systems. *Journal of the Atmospheric Sciences*, 55, 2603–2622.

Weiss, J. (1991) The dynamics of enstrophy transfer in two-dimensional hydrodynamics. *Physica D*, 48, 273–294.

Wood, N., Staniforth, A., White, A., Allen, T., Diamantakis, M., Gross, M., Melvin, T., Smith, C., Vosper, S., Zerroukat, M. and Thuburn, J. (2014) An inherently mass-conserving semi-implicit semi-Lagrangian discretization of the deep-atmosphere global non-hydrostatic equations. *Quarterly Journal of the Royal Meteorological Society*, 140(682), 1505–1520.

Young, M.V. and Clark, M.R. (2018) Development of localized damaging wind gusts associated with a frontal wave and mesoscale vortex across south Wales on 18 May 2015. *Meteorological Applications*, 25, 139–150.

APPENDIX A

Formulae for calculation of $p[\text{TN}]$, given shear vorticity and $-v'_{\text{cold}}$

In CP20, $p[\text{TN}]$ was derived using linear discriminant analysis, as applied to a set of tornadic and non-tornadic analysis points within the two-dimensional parameter space defined by shear vorticity and $-v'_{\text{cold}}$ (see figure 3a of CP20, and Figure 9a of the current article). In this Appendix, we present formulae for the calculation of $p[\text{TN}]$, given shear vorticity and $-v'_{\text{cold}}$. Details of the underlying methodology may be found in Hastie *et al.* (2009). The decision boundary, which is defined as the line of $p[\text{TN}] = 0.5$, is given by:

$$D_{\text{db}} = -(1.2865\ ShearVorticity) - \left(-v'_{\text{cold}}\right) + 23.7230. \tag{A1}$$

D_{db} describes the distance of the given point from the decision boundary. Negative values of D_{db} indicate $p[\text{TN}] > 0.5$, and positive values indicate $p[\text{TN}] < 0.5$. $p[\text{TN}]$ may then be obtained from D_{db} using:

$$p[TN] = 1 - \left\{ \left(\exp\left(0.2384 D_{\text{db}}\right)\right) / \left(1 + \exp\left(0.2384 D_{\text{db}}\right)\right) \right\}. \tag{A2}$$

APPENDIX B

Calculations of primary vortex spacing relative to the unperturbed shear-zone width

Shear-zone width in the 1.5 km and 300 m simulations was estimated by analysis of the 75 m AGL vertical vorticity field in areas exhibiting a general absence of local perturbations in the shear zone. In the 1.5 km model, the shear-zone width was estimated as 4.75 km along the highly two-dimensional part of the shear zone to the southwest of Ireland (Figure 7), using 1×10^{-3} s^{-1} as the lower vorticity limit with which to define the edges of the shear zone (peak values within the shear zone in this region being $\sim 7 \times 10^{-3}$ s^{-1}). According to linear theory (Miles and Howard, 1964), this yields an expected vortex spacing of 35.6 km following vortex sheet roll-up, which compares to a mean primary vortex spacing of 37.9 km (range 31.6–44.3 km) near to vortex C at 1400 UTC. In the 300 m model, estimates are more uncertain due to the presence of perturbations over most of the domain. However, over eastern parts of the Republic of Ireland at 1600 UTC, where the shear zone was relatively free of local perturbations, shear-zone width was estimated as 1.8 ± 0.3 km, equating to an expected vortex spacing of 11.3–15.8 km. This compares to a mean spacing of primary vortices of 14.2 km just east of the Northern Ireland coast at 1500 UTC (Figure 11).

The shear-zone width estimates also reveal that the shear zone is only marginally resolved by the 1.5 km model, being ~ 3 times the grid length, as compared to ~ 6 times the grid length in the 300 m model. It is generally accepted that the effective resolution of a model is in the range 5–8 times the grid length (e.g. Lean and Clark, 2003).

APPENDIX C

Vertical variation of S_{HSI} and its along-front variability

Analysis of horizontal sections at various heights in the 1.5 km simulation shows that S_{HSI} exhibits large gradients in the vertical, with values increasing with decreasing height. Since we invoke the onset of $S_{HSI} < 0$ down-front of the wave centre (as analysed at 1,390 m AGL) to explain the preferential genesis of vortices in this region, the height dependency of S_{HSI} requires further consideration. Within the boundary layer, the height dependency relates to the fact that friction acts to reduce vertical vorticity and increase horizontal convergence along the shear zone, such that the convergence (and therefore bulk cross-frontal confluence) becomes relatively larger than the vorticity with decreasing height. Down-front of the wave centre, a height of transition from positive to negative S_{HSI} can be defined by inspection of values at all model levels between the surface and ~ 3.5 km AGL. The height of this transition is lowest, at around 0.5 km AGL, immediately down-front of the wave centre, that is, where the values of S_{HSI} at 1,390 m AGL were also lowest, and often negative (Figure 6c). This is also where the NCFR updraughts and shear zone tended to be deepest. If the height at which the shear zone becomes indistinguishable from the surrounding vertical vorticity field is taken as the depth of the shear zone, then this varies from ~ 1.0 to 1.5 km along the trailing front, well down-front of the wave centre, and in a separate region up-front of the wave centre, to ~ 2.5 km in the vortex-prone region immediately down-front of the wave centre. The shear zone therefore extends well above the height of transition to negative S_{HSI} in the vortex-prone region ($\sim 80\%$ of the depth of the shear zone being situated within $S_{HSI} < 0$). Conversely the majority, or all, of the shear zone is situated within positive S_{HSI} along the trailing part of the front far down-front of the wave centre, and up-front of the wave centre.

Moore (1985) showed that vortex growth due to pure shearing instability in statically stable environments (as distinct from a buoyancy–shear hybrid instability found in environments exhibiting horizontal wind shear *and* buoyant instability) occurs only in shear zones having aspect ratios greater than unity, where aspect ratio is defined as shear zone depth divided by width. Although this was suggested to be unrealistic for real fronts, the 300 m simulation in the present case shows aspect ratios as high as 2.5–3.0 along the braid regions between primary vortices over the Irish Sea (e.g. as in Figure 15a,b). It is difficult to estimate aspect ratios prior to primary vortex-genesis because increasing shear-zone depth apparently occurs in concert with the development of primary vortices. There is no evidence, however, that the shear zone was systematically wider in the vortex-prone region than elsewhere along the front, suggesting that the aspect ratio was probably largest where the shear zone was deepest. Given the estimated unperturbed shear-zone width of 1.8 ± 0.3 km (Appendix B), and a typical shear-zone depth of ~ 2.0–2.5 km immediately down-front of the wave centre, the aspect ratio of the line was likely close to unity in the vortex-prone region prior to primary vortex-genesis. Therefore, we conclude that both the reduced S_{HSI} (considering mean values over the depth of the shear zone), and the increased aspect ratio, would tend to favour vortex-genesis by the release of HSI in the same region, just down-front of the wave centre.